Solidification and turbulence (non-laminar) during magma ascent: insights from 2D and 3D analyses of bubbles and minerals in an Etnean dyke.

Gabriele Lanzafame[1*], Gianluca Iezzi[2,3], Lucia Mancini[1], Federica Lezzi[2], Silvio Mollo[4], Carmelo Ferlito[5]

[1]Elettra-Sincrotrone Trieste S.C.p.A., SS 14, Km 163.5 in Area Science Park, 34149 Basovizza (Trieste), Italy;
[2]Dipartimento di Ingegneria & Geologia, Università G. d'Annunzio, Via dei Vestini 30, 66100, Chieti, Italy;
[3]Istituto Nazionale di Geofisica e Vulcanologia, Via di Vigna Murata 605, 00143, Roma, Italy;
[4]Dipartimento di Scienze della Terra, Sapienza-Università di Roma, P.le Aldo Moro 5, 00185 Roma, Italy;
[5]Dipartimento di Scienze Biologiche, Geologiche e Ambientali, Università di Catania, Corso Italia 57, I-95129 Catania, Italy.
*Corresponding author: Gabriele Lanzafame email: gabriele.lanzafame@elettra.eu
Corresponding author affiliation: Elettra-Sincrotrone Trieste S.C.p.A., SS 14, Km 163.5 in Area Science Park, 34149 Basovizza (Trieste), Italy;
Email: gabriele.lanzafame@elettra.eu

Keywords: dyke (or dike); bubble; micro-tomography; turbulence (non-laminar); solidification.

ABSTRACT

Numerical models envisage laminar and turbulent regimes in basaltic dykes. In this work, non-laminar characteristics of intrusive magma at Mount Etna have been documented by bi-dimensional (2D) and three-dimensional (3D) analyses conducted on both bubbles and minerals. A 4.3-m-thick aphyric dyke (DK) solidified at depth of 100-300 m below the pristine surface level has been investigated. Textures and fabrics of seven rock samples from dyke rim (DK1) to core (DK7) have been analysed in 2D by using a high-resolution scanner, a transmission optical microscope, and scanning electron microscopy imaging with back-scattered electrons, and in 3D by microfocus X-ray computed tomography.

The amount, size and shape of bubbles, irregularly change from dyke rim to core, in contrast with the limited changes documented for plagioclase (plg), clinopyroxene (cpx), titanomagnetite (timt), and olvine (ol). Bubble and plg contents depict opposite saw-like trends due to solidification from different portions (even as low as a few cm^3) of magma enriched in dissolved H_2O and *vice-versa*. Bubbles with anisotropic shapes (average aspects 3:1) are randomly oriented in space, with strong variations in abundance, dimension, and form. All these features have been attributed to transitional to turbulent, i.e. non-laminar, regimes (Reynolds number > 1000).

Water solubility, volume of bubbles, magma density and viscosity models reveal that at depth > 100-300 m, i.e. P > 10 MPa, a virtual crystal-free magma containing 1 wt.% H_2O intruded, whereas at P < 10 MPa magma significantly degassed and crystallized. Results indicate that a rapid volatile exsolution at very shallow level induced sudden and marked crystallization, coupled with increase of viscosity and rapid deceleration or even arrest of magmatic suspension; the bubbles were frozen in, whereas crystals continued to grow under the effect of cooling rate increasing from inner to outer dyke portions. Despite the low H_2O content, the trachybasaltic magma was close to its *liquidus* temperature and the estimated ascending velocity of a few m/s led to hypothesize transitional to turbulent regimes during the emplacement of the dyke.

INTRODUCTION

The ascent of magmas to shallow crustal levels occurs mainly along dykes that are categorized as discrete, vertical, sheet-like bodies. When the pressure at the summit of a magmatic reservoir overcomes tensile resistance of overlying rocks, failures can develop by coalescence of cracks under the stress induced by pressurized volatiles (gas cap of H_2O and CO_2) and fluids (melt ± dissolved volatiles ± minerals ± bubbles). Then, failures propagate upwards responding to the mechanical properties of overlying rocks, regional, and local stress fields, as well as the fluid-mechanical behaviour of injected magmas (Pollard, 1973, 1976 and 1987; Spera, 1980; Delaney *et al.*, 1986; Lister & Kerr, 1991; Rubin, 1995; Gudmundsson *et al.*, 1999; McLeod & Tait, 1999; Menand & Tait 2001; Gudmundsson, 2006; Acocella & Neri, 2009; Geshi & Neri, 2011; Maimon *et al.*, 2012; Daniels *et al.*, 2012; Mangan *et al.*, 2014; Rivalta *et al.*, 2015; Gonnerman & Taisne, 2015 and references therein).

Most dykes develop near vertically in the host rocks and, rarely, produce eruptions. This depends on the physico-chemical conditions of magma and host rock, such as the chemical composition, initial temperature (T), pressure (P), volatile and/or crystal contents and kinetic effects determining nucleation and growth of mineral phases, degassing, and outgassing. Kinetic effects are governed by heat transfer from magma to the surrounding host rock and the ascent rate imposed by magmatic overpressure and density contrast between magma and cross cut rock(s) (Spera, 1980; Bruce & Huppert 1990; Carrigan *et al.*, 1992; Rubin, 1995; Carrigan, 2000; Jaupart, 2000; Pinel & Jaupart, 2004; Taisne & Jaupart, 2009; Taisne *et al.,* 2011; Maccaferri *et al.*, 2011; Zuan Chen *et al.*, 2011; Maimon *et al.*, 2012; Yamato *et al.*, 2012 and 2015, Mangan *et al.*, 2014; Gonnerman & Taisne, 2015; Rivalta *et al.*, 2015 and references therein).

Efforts spent on dyking allowed to bracket these complex processes that are central for many topics, like lithospheric evolution, generation of new crust, lifetime of volcanoes and related hazards. However, several theoretical aspects of dyke emplacement still need to be corroborated

(Maccaferri *et al.*, 2011; Galindo & Gudmundsson, 2012; Daniels *et al.*, 2014; Gonnerman & Taisne, 2015; Rivalta *et al.*, 2015). One central question is the fluid-dynamic regime in dykes. Theoretical and numerical models foresee both laminar and non-laminar regimes (Huppert & Sparks, 1985; Emerman & Turcotte, 1986; Spence & Turcotte, 1990; Carrigan, 2000; Jaupart, 2000), despite turbulence in dykes is only suggested by crude field observation (Kille *et al.*, 1986).

Pioneering bi-dimensional (2D) textural and fabric studies of minerals and bubbles unveiled both petrological and rheological magmatic processes in dykes (Teall, 1884; Queneau, 1902; Holmes & Iarwood, 1929; Quinn, 1943; Winkler, 1948; Campbell & Schenk 1950; Cashman, 1992; Sigurdsson, 2000; Mangan *et al.*, 2014). These studies were followed by more quantitative 2D investigations (Gray, 1970 and 1978; Komar, 1972 and 1976; Ikeda, 1977, Howard, 1980; Shelley, 1985; Wada, 1992; Hastie *et al.*, 2011 and 2013), revealing variations in size and shape of minerals and bubbles, as well as of fabric moving from central to external parts of dykes. In the last decades, dykes have been largely investigated by three-dimensional (3D) anisotropic magnetic susceptibility (AMS) (Ernst & Baragart, 1992; Callot *et al.*, 2001; Herrero-Bervera *et al.*, 2001; Femenias *et al.*, 2004; Aubourg *et al.*, 2008; Eriksson *et al.*, 2011; Bjarne *et al.*, 2012; Andersson *et al.*, 2016 and reported references), to a lesser extent by 2D textures combined with magnetic properties (Poland *et al.*, 2004; Clemente *et al.*, 2007; Philpotts & Philpotts, 2007; Hastie *et al.*, 2013). Conversely, a few studies on volcanic rocks have been performed using other 3D methodologies to investigate crystal lattice preferred orientation such as EBSD (Bascou *et al.*, 2005), neutron diffraction (Walter *et al.* 2013) and micro-computed tomography (Álvarez-Valero *et al.*, 2016).

The orientation of magnetic tensor mainly depends on the texture and fabric of iron-bearing crystals with relevant magnetic signals like titanomagnetite (timt), moderate for biotite (bt) and amphibole (amph), and low for plagioclase (plg), clinopyroxene (cpx) and olivine (ol). Thereby, AMS is not suitable to measure absolute dimensions and shapes of bubble and mineral populations, recording only the late stage of deformation (Iezzi & Ventura, 2002; Cañón-Tapia & Chàves-Àlverez, 2004; Cañón-Tapia & Herrero-Bervera, 2009). Magma dynamics in dykes can be also

successfully investigated by mineral compositional variations (Chistyakova & Latypov, 2009; Tartese & Boulvais 2010; Mollo *et al.* 2011 and 2012; Scarlato *et al.*, 2014 and previous works). The combination of textures, fabrics, and compositions per each phase is indeed the most complete strategy to reconstruct the solidification paths of magmas feeding dykes. Surprisingly, dykes are scarcely investigated by modern microchemical and 2D imaging methods, as well as 3D imaging techniques. Only recently, X-ray computed tomography has been applied to dacitic magmas (Álvarez-Valero *et al*., 2016) with obvious compositional, textural, and rheological differences with respect to the trachybasaltic magma analysed here.

In this study, the textural and fabric attributes of seven rock samples representative of the core-to-rim internal variability of an Etnean dyke have been investigated to complement major and trace element changes previously documented for plg, cpx and timt (Mollo *et al.*, 2011; Scarlato *et al.*, 2014). The rock samples have been analyzed either by 2D methods (on polished rock surfaces and thin sections) and 3D imaging using X-ray computed microtomography (X-ray μCT). The size, shape, and orientation of bubbles and minerals allow to reconstruct the solidification behaviour of magma and appear to confirm the fluid-dynamic scenario suggested by theoretical models. Similar investigations can be extended to other dykes or lavas, to better understand the mechanisms responsible for the transport of magmas at shallow crustal levels and volcanic eruptions.

THE ETNEAN DYKES

Geological Setting

Mt. Etna is an active stratovolcano located in eastern Sicily (Italy) and is characterized by effusive and strombolian activity associated to persistent degassing from its four main craters (Monaco *et al.* 1997; Ferlito & Lanzafame, 2010; Ferlito *et al.*, 2014). The main edifice of the volcano built in the last 220 ky (Gillot *et al.* 1994; Tanguy *et al.*, 1997; De Beni *et al.* 2005; Tanguy *et al.*, 2007; Branca *et al.* 2008) and developed through four major phases: Ancient Alkaline Centers (AAC; 220–120 ka), Trifoglietto (80 - 60 ka), Ellittico (60 - 15 ka) and Recent Mongibello

(15 ka to present) (Cristofolini *et al.* 1979; Romano, 1982; Gillot *et al.* 1994; Catalano *et al.* 2004; Monaco *et al.* 2005 and references therein). On its eastern side the current edifice is characterized by the Valle del Bove depression, bordered on its western part by the high reaches of the volcano and on its northern and southern sides by steep walls formed by remains of the Trifoglietto and Ellittico products (Romano 1982; McGuire 1982; Lanzafame & Vestch 1985; Ferlito & Cristofolini 1989; Calvari *et al.* 1994, Coltelli *et al.* 1994, D'Orazio *et al.* 1997; Monaco *et al.*, 2010). Several dykes outcrop over these steep walls, displaying portions of the ancient shallow plumbing system feeding the various eruptive centers (cf. Ferlito & Nicotra, 2010).

Features and sampling of the dyke

On the southern wall of the Valle del Bove, at the head of the ample gully named Canalone dei Faggi at about 1,700 m a.s.l. (Fig. 1), several dykes are observable with common features: thickness of a few meters, near vertical attitude, sharp contacts with wall-rocks, absence or very limited content of observable crystals (aphanitic texture), moderate amounts of elliptical bubbles with size up to 10-20 mm distributed in bubble-rich and -poor patches, and absence of bubbles. The bubbles do not follow any textural trends from rim to core and primarily form eddies or vortex with diameters from several centimetres to a few decimetres.

We focused on a 4.3 m thick dyke, labelled DK, which intruded lava and pyroclastic sequences ascribed to the Ellittico activity before 15 ky. This portion of the dyke was originally located at a depth of 100-300 m below the ground surface (Mollo *et al.,* 2011). The dyke appears as a single body likely originated during one single magmatic pulse, cutting pre-existing rocks with very sharp contacts, without any contaminations and/or comb layers (Fig. 1). From outermost to innermost DK portions, seven samples were collected with sampling distance of ~35 cm. These prismatic samples are oriented coaxially to the field: Z is the vertical direction, X is the thickness (rim to rim) and Y is the horizontal direction of DK (Fig. 1). The sampled rocks have edges of about 100/200, 100/200 and 50/100 mm. Each sample was then cut normally to the dyke walls such

to expose the representative Z-X surfaces (Fig. 1). Then, seven surfaces (or portions of them) with areas in the order of 10^3 mm^2 were polished for statistic relevant mesoscopic observations. The short and long sides of these sections are coaxial with Z and X directions, respectively. We collected these samples in the half-width right part of the dyke, assuming that the rocks are representative of the entire dyke. We are aware that some dykes may show a non-symmetric fabric from rim to rim (Femenias *et al.*, 2004; Nkono *et al.*, 2006) but, in this case, the overall thickness of the dyke is limited at the spatial scale showing clear symmetric characteristics.

Mineralogy and geochemistry

The seven rock samples object of this study were already investigated by Mollo *et al.* (2011 and 2013) and Scarlato *et al.* (2014). The DK dyke is trachybasaltic with (wt.%) SiO_2=48.6 (±0.3), TiO_2=1.9 (±0.1), Al_2O_3=16.9 (±0.2), FeO=11.3 (±0.2), MnO=0.2 (±0.1), MgO=4.2 (±0.1), CaO=10.4 (±0.1), Na_2O=3.8 (±0.2), K_2O=1.6 (±0.1), P_2O_5=1.2 (±0.1). The phase assemblage of the dyke comprises ol, cpx, plg, and timt where ol was introduced to the original melt as xenocrystals (Mollo *et al.*, 2011). Plg, cpx and timt compositions progressively change from dyke core to rim (Mollo *et al.*, 2011 and 2013). Specifically, albite (Ab), diopside (Di) and ulvospinel (Usp) increase, counterbalanced by decrease of anorthite (An), Tschermak (Ts) and magnetite (Mg) (Fig. 1). The increasing amounts of Ts from dyke core to rim are also accompanied by increasing concentrations of rare earth elements in cpx (Fig. 1) (Scarlato *et al.*, 2014).

MATERIALS AND METHODS

2D imaging, processing, and analysis

The mesoscopic polished surfaces with areas of 10^3 to 10^4 mm^2 were prepared to expose phases with maximum dimension > 1 mm. Thin sections show 2D textural attributes at a 1:1 scale acquired by high-resolution scanner (HRS), at 2.5× and 10× magnifications (parallel and cross polarizers) with a transmission optical microscope (TOM), and a scanning electron microscope with

back-scattered electrons (BSE-SEM) at 100× to 3000× magnification. HRS analyses were performed with a high resolution Epson V750 Pro scanner, TOM investigation were carried out with a Zeiss Axioscope optical microscopy, both installed at the Dipartimento di Ingegneria & Geologia of the University G. d'Annunzio (Chieti, Italy), whereas for BSE-SEM analyses a Jeol-JXA8200 scanning electron microscope equipped with EDS and installed at HPHT Laboratory of Experimental Volcanology and Geophysics of the Istituto Nazionale di Geofisica e Vulcanologia (INGV) in Rome (Italy) was used. Variable areas and related magnifications of digital images allow to statistically constrain all phases with centimetric to micrometric sizes, avoiding over- and under-samplings effects (low counting for few large objects). The more abundant phases have been scaled thus accounting for the different magnifications.

The techniques employed for textural quantifications on the basis of phase sizes are summarized in Table 1. Nine images per sample with a total of sixty-three digital images were performed following the protocols and procedures reported in previous studies (Higgins, 2006; Iezzi *et al.*, 2008, 2011 and 2014; Lanzafame *et al.*, 2013; Vetere *et al.*, 2013 and 2015a and references). 2D image processing and analysis were performed using the Image Pro-Plus 5.0 commercial software. Each image obtained at various magnifications was first transformed in grey levels (0: black and 255: white) and calibrated to a mm scale. After the use of a *median filter* in order to remove noise, each phase (bubbles and crystals) with its peculiar grey levels was identified, using a grey range as narrow as possible to reproduce the grey levels. After that the phases were reproduced in false colours, they were segmented and automatically counted.

Objects attributed to each phase were characterized considering their corresponding equal-area ellipses. We calculated the phase abundance expressed as area% (ratio between the area occupied by the investigated phase and the total area of the sample section), the number density (defined as the number of objects per unit area, #/mm^2), the object size (considered as the long and short axes of the ellipses and their ratio) and the orientation of the long axis with respect to the X direction (see Fig.1).

Bubbles having sizes > 0.1 mm were quantified by means of images from HRS and TOM. Since crystal sizes never exceed ~0.2 mm they were measured on BSE-SEM pictures (see below). Plg aggregates along the longest axis, preventing the accurate identification of single crystals. In contrast, cpx, timt, ol, and bubbles can be sharply identified and quickly measured as single objects. The quantitative textural 2D data were not treated with stereological conversion. A schematic view of the workflow used in the 2D image processing and analysis is represented in Fig. 2.

3D imaging, processing, and analysis

Seven DK samples (see Table 2) were imaged by laboratory X-ray μCT using the TomoLab station at the Elettra synchrotron light facility in Basovizza (Trieste, Italy) (Mancini *et al.*, 2007; Polacci *et al.*, 2009; TOMOLAB, 2010). The TomoLab is equipped with a sealed microfocus X-ray tube operating in a Voltage range from 40 to 130 kV, a maximum current of 300 μA and a minimum focal spot size of 5 μm. The detector consists of a full frame CCD imager (4008 × 2672 pixels) coupled to a gadolinium oxysulphide scintillator by a fiber-optic tape. The water-cooled camera has a 12-bit dynamic range, and an effective pixel size of (12.5 × 12.5 μm^2). Due to the cone-beam geometry, it is possible to achieve a spatial resolution close to the focal spot size, on samples from a few millimeters to a few centimeters in size. The experimental parameters used for the X-ray μCT scans are reported in Tab. 2. Scans for DK1 and DK5 were obtained with a pixel size of 6.25 μm while scans for samples DK2, DK3, DK4, DK6 and DK7 were acquired with a pixel size of 8 μm. The slice reconstruction was performed using the commercial software COBRA (Exxim) based on the Feldkamp algorithm (Feldkamp *et al.*, 1984).

3D image processing and analysis of the seven imaged samples were performed using the *Pore3D* software library custom-developed at Elettra (PORE3D, 2009; Brun *et al.*, 2010; Zandomeneghi *et al.*, 2010), which allows to conduct a quantitative microstructural analysis of porous and multiphase systems. The software includes tools for filtering and segmentation of digital images, procedures for the analysis of morphology, texture, and anisotropy as well as for the

skeletonization and skeleton analysis functions to extract topological information. The 3D visualization (through surface and volume rendering procedures) of reconstructed and processed volumes was done employing the commercial software VGStudio MAX 2.0 (Volume Graphics). The *Pore3D* software was also used to reduce ring artefacts from the reconstructed axial slices (Sijbers & Postnov, 2004; Brun *et al*., 2010; Brun *et al*., 2011).

Quantitative analyses were performed on suitable Volume of Interest (VOI), extracted from each imaged sample with the aim to detect the representative structures of the rocks (Table 3). In order to verify the representativeness of the VOIs, Representative Elementary Volumes (REVs) were determined. A REV is defined as the minimum volume large enough to enclose a representative amount of the sample heterogeneity (Gitman *et al*. 2007; Zandomeneghi *et al*., 2010). For each sample, we considered the bubble and timt volume fraction as the parameter for REV determination and applied the box-counting method (Al-Raoush & Papadopoulos, 2010; Zhang *et al*., 2012).

VOIs having size larger than the determined REVs were then extracted and filtered to remove noise and enhance edges using an "anisotropic diffusion filter" (Weickert, 1998). The next step was the segmentation of the images to obtain binary volumes containing the different classes of the phase of interest. Thresholding was performed using the automatic MultiOtsu method (Otsu, 1979). For each sample, we extracted two binary datasets corresponding to bubbles and timt, the less and most dense phases with respect to the DK groundmass. Segmented images were then processed applying various cycles of erosion and dilation in order to remove noise and outliers background objects < 3-5 voxels (Serra, 1982).

Since samples show bubbles and timt in contact with the border of the VOIs, analyses were performed on two datasets: i) VOIs containing all the objects, in order to have a measurement of the total amount and ii) VOIs in which the objects touching the image margins were suppressed, considering only the morphometric values of un-truncated objects. We applied the *Basic Analysis* module of the *Pore3D* software (Zandomeneghi *et al*., 2010) to obtain bubbles and timt density

(number of voxels of each phase *vs* the total number of voxels), specific surface area (surface area of all phase divided by the total VOI), integral of mean curvature (index resuming abundance of convex *vs* concave shapes; Russ & De Hoff, 1986) and Euler characteristic (index scaling with the network connectivity of a given phase; Odgaard & Gundersen, 1993; Ohser & Mücklich, 2000) (Table 3). All bubbles and timt, identified using the concept of maximal inscribed spheres (Hildebrand & Rüegsegger,1997 ; Baker *et al*., 2012), were then labelled and analysed, calculating the number of elements, volume, sphericity, aspect ratio and diameter of the maximal inscribed sphere. The spatial relations of the objects within the samples were then investigated calculating the isotropic distribution and preferential orientation of bubbles and timt.

The connectivity of bubble networks was investigated by a skeletonization approach (Lindquist & Lee, 1996). The skeleton can describe the connectivity and tortuosity of the bubble network since it can be intuitively considered as the 1D representation of the "spine" of a 3D object. Due to hardware-related computational limits, the skeletonization was performed on sub-VOIs with size of 500×500×500 voxels still having REV characteristics. After visual inspection, we selected the *LKC* skeletonization function (Lee *et al.*, 1994). Two cycles of 3D median filtering were run on the segmented images of bubbles in order to smooth their borders before the computation. After skeletonization, an iterative pruning of all branches with sizes < 20 voxels was applied. The application of smoothing and pruning procedures allow to remove unnecessary branches and nodes which do not represent the real connectivity frames. A graphical summary of the most important 3D image processing and analysis steps adopted is reported in Fig. 3.

RESULTS

2D texture and fabric

2D textural features of phases are summarized in Fig. 4 and detailed information are reported in the supplementary materials (Figs. 4Sa-g). From dyke rim (DK1) to core (DK7), the most important characteristics are: i) bubbles size (long axis of equal-area ellipse) > 0.1 mm and

crystal size < 0.1 mm for most of the minerals (the crystal size never exceeds 0.2 mm), ii) bubbles show heterogeneous distributions, shapes, and orientations that contrast with the high homogeneity of crystals and iii) the glass matrix is absent or possibly corresponds only to a few area% around plg rims (Figs. 4 and 4S).

Area%, size, number density, shape, and orientation of bubbles do not follow any monotonic trend (see Figs. 4 and 4S). At the macroscopic scale, DK1 is the only sample containing a great number of sub-millimetric (size > 0.1 and < 1 mm) bubbles, whereas the other samples are mostly characterized by large bubbles (size > 1 mm). Bubbles with lower dimensions tend to be more equant than larger ones. Bubbles in DK5 and DK7 are weakly deformed with rounded contours. DK2 contains bubbles with high anisotropic and irregular shapes, whereas intermediate shapes are observed in DK1, DK3, DK4 and DK6. The fabric of bubbles is oriented nearly coaxial to the vertical Z direction (see Fig. 1) in DK2, DK4, DK5, and DK6, at 30/60° from Z for DK3 and along X for DK6 (Figs. 4 and 4S). These observations from digital scanned images are in agreement with those in the field and from polished rock samples.

The texture and fabric of minerals display weak variations from dyke rim to core (Figs. 4 and 4S). Plg is by far the most abundant phase and occurs as attached crystals along their longest directions. Cpx is the second most abundant mineral with a prismatic contour. The amount of timt is low and larger crystals (maximum size of about 100 µm) exhibit irregular boundaries resulting from the attachment of tiny crystals (maximum size of a few µm). Ol occurs invariably as small equant and faceted crystals (Figs 4 and 4S).

The area% of phases observed by HRS, TOM, and BSE-SEM analyses conducted at progressive higher magnifications are summarized in Table 1 and plotted in Fig. 5a. The abundance of bubbles from dyke rim to core exhibits an irregular saw-like trend (Fig. 5a). Bubbles with size > 1 mm are extremely low (0.1 area%) in DK1 whereas bubbles with size > 0.1 and ≤ 1 mm are scarce (< 2 area%) in the inner dyke portions (DK5, DK6, and DK7) and more abundant (9.1 to 12.8 area%) in DK1, DK2, and DK4 (Table 1).

The values of plg area% shows an opposite trend relative to bubbles. When the amount of bubble decreases, the abundance of plg increases and *vice versa*. A similar but less marked saw-like trend is also observed for cpx (Fig. 5a). The number density of cpx changes from dyke rim to core (Table 1 and Fig. 5b), suggesting that the margin of the dyke (DK1) was rapidly cooled at the contact with the walls of the host rock (Mollo *et al*., 2011). Ol has a low abundance and crystal length of a few tens of micrometers (Table 1, Figs. 4 and 4S).

3D texture and fabric

3D bubble textural parameters are reported in Table 3 and graphically represented in Figs. 6a and 6b. The volumetric abundance of bubbles follows a complex saw-like trend (Fig. 7a) similar to that determined by the 2D analysis (Fig. 5a). Samples DK1 and DK6 show the lowest bubble contents (~11 vol.%), while sample DK5 has the highest bubble amount (~23 vol.%). The abundance of bubbles obtained by 3D analysis is comparable with 2D data for sample DK1, DK2, DK3, DK6 and DK7. In contrast, samples DK4 and DK5 show differences (see discussion below). The overall trend depicted by the number of bubbles per unit volume is also similar to that measured in 2D (Figs. 5b and 7b).

Timt is the only crystalline phase that has been resolved by microfocus X-ray μCT due to its relative high contrast with respect to plg, cpx and ol. Differently from rough 2D data, 3D measurements show that the abundance (2-2.5 vol.%) of timt remains practically constant from dyke rim to core (Table.3).

Amount and number of bubbles

The abundances of bubbles determined by 2D and 3D analyses are similar (Fig. 8). DK1 shows minimum discrepancy of ~1%. DK2, DK3, DK6, and DK7 show moderate differences lower than ~3%. Conversely, discrepancies up to ~8% are observed for DK4 and DK5 (Tables 1 and 2, Fig. 8) and can be ascribed to the heterogeneous distribution of bubbles in the different portions of

the samples (Figs. 4, 4Sd, 4Se and 9). The X-ray μCT analysis was in fact focused mostly on the volumetric portions of DK4 and DK5 that are enriched in bubbles, whereas 2D data from thin sections refer to both bubble-rich and bubble-poor areas (Figs. 4, 4Sd and 4Se). This interpretation is corroborated by the almost identical values of 2D (11.2 area%) and 3D data (10.9 vol.%) measured for the most homogeneous DK1, showing a high number of small bubbles at the scale of several cm^2 and cm^3 (Tables 1 and 3, Figs. 4Sa, 6a, 6b and 9). In contrast, DK4 is strongly heterogeneous for what concerns the distribution and size of bubbles, with the coexistence of bubble-rich and bubble-poor areas in the order of several 10^3 mm^2 (Figs. 4, 4Sd and 9). A similar conclusion holds for the number of bubbles per area and per volume determined from dyke rim to core (Figs. 5b and 7b). These trends are similar, suggesting that DK1 is radically different from the other dyke samples. In other words, the dyke rim contains a great number of small bubbles only at the contact with the country-rock (a-few-dm-thick layer) in which large bubbles are virtually absent (Figs 4a, 5b, 6a, 6b and 7b). The good match between 2D and 3D determinations indicates that the total amount of bubbles is comprised between 10 and 30 area% and/or vol.% (Table 1, Figs. 5 and 7).

Size and shape of bubbles

The majority of bubbles, counted as equal-area ellipses in 2D on the Z-X plane (Fig. 1), show length (longest axis of equal-area ellipse) lower than 4 mm, with the exception of DK1 containing bubbles < 2 mm (Fig. 10). On average, linear regression fits (blue lines in Fig. 10) quantify a ratio of bubble length to width (shortest axis of equal-area ellipse) of 3:1 (except for DK6). These 2D trends are further confirmed by the relationship between length and aspect ratio. The latter parameter varies between 1 and 4 and is not correlated with the bubble size (Fig. 10).

Within the limits of a spatial resolution of the order of 10 μm, X-ray μCT provides a quantitative determination for the bubble size and shape, also validating 2D measurements. 3D analysis reveals that DK7 and DK1 have the largest (0.22 mm^3) and smallest (0.002 mm^3) bubble

volumes, respectively. The other samples have variable bubble volumes in the order of $10^{-1}/10^{-2}$ mm^3, but no clear trends are observed from DK1 to DK7 (Table 3). 3D bubble shapes are reported in Table 3, calculated as the ratio between the minimum and the maximum axis of each blob from 0 (line) to 1 (sphere). Results indicate that samples contain elongated bubbles (average aspect ratios between 0.22 and 0.38 or 4.5:1 and 2.6:1), but DK1 and DK5 are the most anisotropic. 3D size and shape distributions of bubbles are reported in Fig. 11. The average ratios between length and width of these bubbles are slightly lower than those observed for 2D data but, indeed, are invariably close to 3:1 (Figs. 10 and 11). Hence, in this case, typical sizes and shapes of bubbles were consistently captured also by 2D method.

The variation of bubble shape as a function of size from 3D tomography indicates that a great number of small bubbles is underestimated by 2D image analysis (Figs. 10 and 11). The most part of 3D bubble shapes have aspect ratios around 3:1 (blue regression lines in Fig. 11), in agreement with their average values (Table 3) and with 2D data (Fig. 10). However, a minor part of bubbles has extremely high ratios (right plots in Fig. 11) that can be interpreted as unconnected channels with maximum lengths < 2 mm (Figs. 10 and 11). These channels are also observed in the thin section of DK3 sample (Fig. 4Sc), possibly indicating that a minor part of exsolved gas was in connection with large bubbles. The number of these channels is high in DK1, DK2, and DK3, moderate in DK4 and DK5, and low in DK6 and DK7 (Fig. 11). The presence of unconnected micrometre-sized channels in DK2 and DK3 and to a less extent in DK4, DK5, and DK6, suggests at least two events of gas exsolution (Fig. 11). Merging 2D and 3D data, it is found that the bubble size is comprised between 0.1 and 10 mm, with only DK1 showing bubble size < 1 mm (Table 1). Conversely, the bubble shape is close to 3D ellipsoids with axial ratio of about 3:1:1 (Figs. 10 and 11).

Distribution and orientation of bubbles

The isotropic (I) and the elongation (E) 3D indexes evidence the tendency to develop (or not) a fabric (Tab. 3). These calculations were performed excluding in VOI analysis the bubbles with touching edges that were truncated. The index I represents the similarity of a fabric to a uniform distribution (Benn, 1994). In dyke samples, bubbles exhibit a high (but incomplete) isotropic distribution (I = 0.70-0.78) (Table 3), in agreement with the presence of bubble-rich and bubble-poor areas (Figs. 4, 4S, 6a, 6b and 9). The preferred bubble orientation is quantified by the elongation, that is invariably low (E = 0.03-0.10) from dyke rim to core. This is apparently in contrast with 2D images (Figs. 4 and 4S), where bubbles are arranged along several preferred directions. However, 2D bubble orientations are, indeed, sub-fabrics reflecting only thin rock portions that disappears when averaged in a 3D rock volume, i.e. there are not preferential bubble orientations. This finding suggests that 2D analysis is not suitable to determine the rock fabric. Thus, 3D upshots represent the best method to outlining that bubbles are not perfectly homogeneous distributed and that preferential bubble alignments are lacking. Notably, this latter feature differs with what is expected for 3:1:1 bubbles moving in a laminar flow medium.

Connection and coalescence of bubbles

The connectivity density is a proxy for determining the amount of connected and unconnected bubbles in dyke samples. Specifically, DK1 shows the lowest value of connectivity density (Table 3), coherently with the highest amount of unconnected channels (Fig. 11). However, the connectivity density is always near to zero, indicating that blobs are scarcely connected in dyke samples. Bubbles are not perfectly equally distributed within the rocks, allowing to identify different subvolumes for each VOI and to perform LKC skeletonization. The minimum (-10.45) and maximum (1.7) values of connectivity density are given by subvolumes from DK1 and DK5, respectively. This suggests that, with respect to the dyke margin (DK1), the scarce amounts of connected bubbles in the inner portions of the dyke (from DK2 to DK7) were formed at the early stage of the magmatic intrusion. Moreover, coalescence attributes were estimated by the integral of

the mean curvature (*Mv*), resolving the dominance of convex or concave structures. Positive *Mv* values for all the samples point out the dominance of convex surfaces due to the abundance of isolated bubbles, especially in DK1 that, indeed, shows the highest number of bubbles (Table 3).

Amount, number, size, shape, and distribution of titanomagnetites

From DK1 to DK7, the amount and number density of timt are low, showing modest variations for both 2D (3.9-7.7 area.% and 400-1100 #/mm^2) and 3D methods (2-2.5 vol.% and 52-112 #/mm^3) (see Tables 1 and 3, as well as Figs. 4, 4S, 5, 6, 7 and 8). The distribution of timt is almost homogeneously in the samples ($I \geq 0.88$). Preferential crystal orientations ($E \leq 0.06$) are not observed due to the isotropic shape on minerals (Table 3). Consequently, the timt texture does not change from the outermost to innermost portions of the dyke (contrarily to what observed for bubbles).

DISCUSSION

Solidification process

Minerals show only minor variations of the textural attributes in concert with moderate and almost linear changes in composition of plg, cpx, and timt from DK1 to DK7 (Fig. 1; Mollo *et al.*, 2011; Scarlato *et al.*, 2014). Conversely, the abundances of plg and cpx, as well as the number per area of cpx do not linearly change (Tables 1 and 3, and Figs. 4, 4S, 5, 6 and 7). Texture of crystalline phases strongly contrasts with irregular variations in amount, size, shape, distribution, and orientation of bubbles (Tabs. 1 and 3; Figs. 4, 4S, 5, 6, 7, 10 and 11). At the shallow portions of Mt. Etna feeding system, H_2O controls profoundly magma solidification and rheology (Mollo *et al.*, 2015a; Perinelli *et al.*, 2016), being the most important dissolved volatile species and the most abundant gas in bubbles (Del Gaudio., 2010; Giacomoni *et al.*, 2014; Fiege *et al.*, 2015; Vetere *et al.*, 2015b). Most of the observed bubbles, especially those of large dimensions, formed before the crystallization of minerals when the magma was substantially in a liquid state or highly ductile.

The aphyric character of the dyke samples, the moderate to tiny size (< 0.1-0.2 mm) of crystals, and the average high number of crystals per area or volume (Figs. 4, 4S, 5 and 6) point out straightforwardly to an initial crystal-poor intrusion. Hence the magma was injected in the host rock under super-heated condition or close to its *liquidus* temperature. In turn, crystals mostly nucleated and grew during ascent of DK magma by both decompression-induced degassing (Hammer, 2008; Fiege *et al.*, 2015 and reference therein) and cooling (Iezzi *et al.*, 2008; 2011; Mollo *et al.*, 2011; Vetere *et al.*, 2013 and 2015b) processes. At the time of emplacement, the sampled dyke level was located at 100-300 m depth (Mollo et al., 2011). Indeed large bubbles grow below this level, whereas tiny bubbles resulted from a second minor event of exsolution (Figs. 10 and 11), occurred close to this shallow level. The exsolution of H_2O induced also the onset nucleation of plg and cpx. All these processes cooperated to rise the viscosity of magma, as well as decelerating and halting the intrusion. The solubility and exsolution of H_2O is markedly determined by pressure decrease, in turn induced by magma ascent and to a minor extent by temperature. In contrast, pressure and temperature changes control crystal nucleation and growth (Hammer, 2008; Iezzi *et al.*, 2008 and 2011; Vetere *et al.*, 2013 and 2015a; Fiege *et al.*, 2015 and references therein).

The irregular saw-like trend of bubbles from dyke core to rim is a proxy for the distribution of H_2O-poor and H_2O-rich magma portions (1-10 cm^3) (Figs. 5a and 7a) producing bubble-poor and bubble-rich dyke portions. Similarly, the negative correlation between plg and bubble abundances can be ascribed to the role of H_2O at the time of dyke emplacement (Fig. 5). Plg nucleation was driven by decompression-induced degassing, at a moderate to high degree of undercooling forming tiny crystals, high number of crystals per area, and frequent self-aggregation of crystals (Figs. 4, 4S and 5). A similar interpretation holds for cpx due to its saw-like trend similar (but less marked) to that of plg. If the initial nucleation of plg and cpx would be induced only by cooling, the number of crystals per area should be very high at the dyke rim to progressively decrease towards the core, as expected upon the effect of a variable cooling rate condition (Cashmann, 1992; Hammer, 2008; Vetere *et al.*, 2013 and 2015b). The decreasing trend of the number per area of bubbles and cpx, as

well as the formation of tiny bubbles in DK1 are indicative of the effect of cooling only in proximity of the dyke margin (Figs. 4, 5, 6 and 7).

Fluid-dynamic mechanism

A nodal characteristic of the dyke is the irregular distribution of exsolved H_2O wt.%, i.e. bubbles. Both 2D and 3D textural and fabric analyses clearly evidence the irregular pattern of bubbles from dyke rim to core. 2D data reveal variable bubble orientations (especially of the larger ones) coherently with the absence of preferred orientation of bubbles with average 3:1:1 aspect ratio in 3D (Table 3, Figs. 4, 4S,, 6a, 6b, 10 and 11). These distributions result from movement and deformation of bubbles not only along the vertical Z but also along X and Y directions, suggesting that magma emplacement occurred by a non-laminar behaviour due to transitional and/or turbulent regimes before or at the early stage of plg and cpx crystallization. In a laminar flow, the longest axis of bubbles must orient in the same direction of transport, here the Z axis (Fig. 1). In parallel, the aspect ratio of bubbles must increment from central to outer fluid portions (Gonnerman & Mangan, 2012; Mangan *et al*., 2014). These classical features of laminar flows are lacking. The textural and fabric characteristics of most part of bubbles can be ascribed only to transitional and/or turbulent fluid conditions (Tables 1 and 2, Figs. 4, 4S, 5, 6a, 6b, 9, 10 and 11).

This conclusion is validated by the apparent discrepancies in 2D and 3D bubble contents measured for DK4 (Fig. 9). The polished surface of this sample displays, in an area of only 8×10^3 mm^2, the coexistence of portions with bubbles having highly variable amounts, sizes, and shapes. A high strain favoured high amounts and anisotropic shapes of bubbles (for instance at the margin of adjacent vortexes). The opposite is plausible for portions of magma subjected to relative low strains. It is also reasonable that the transient and/or turbulent dynamics were limited or even lacking at a few tens of centimeters next to the dyke margin, due to the major effect of heat transport (Figs. 4a, 6a and 6b). The presence of transitional to turbulent regimes also limits temperature changes along

the X and Y dyke directions, as well as the development of fast cooling rate conditions (Spera, 1980; Huppert & Sparks, 1985; Spence & Turcotte, 1990; Carrigan, 2000).

Physical constraints

Thermometric estimates from dyke core to rim indicate that the early crystallization of plg and cpx occurred at 1,119 ± 19 °C and 1,126 ± 26 °C, respectively (Mollo *et al.*, 2011). These comparable thermal conditions agree with the similar crystal dimensions (< 0.2. mm) measured for plg and cpx across the dyke (Figs. 4 and 4S). Furthermore, the total H_2O content dissolved in the magma has been estimated to be 1.6 ± 0.3 wt.% at fO_2 of NNO+0.9 ± 0.9 (Mollo *et al.*, 2011). The emplacement pressures have been computed in this study by considering field observations (see the supplementary excel spreadsheets). Volcanic rocks at Mt. Etna are trachybasalts emitted principally as dense lavas and secondarily as scoriae. We thus considered three densities of 2,000, 2,500, and 3,000 kg/m^3 to bracket the pressure conditions as a function of depths below the original dyke surface (100/300 m depth):

$$P = \rho \times d \times g,$$

where ρ is the density (kg/m^3) of the overlying rocks or dyke magma, d is the dyke width (X direction in Fig. 1), and g is the gravity acceleration (m/s^2). This calculations envisage a maximum and conservative range of pressures between 2 MPa (ρ of 2,000 kg/m^3 at 100 m) and 9 MPa (ρ of 3,000 kg/m^3 at 300 m) (Fig. 12).

The solubility of water in magma and the volume of exsolved gas phases have been computed using the models of Papale *et al.* (2006) and Solex (Whitam *et al.*, 2012), assuming closed-system conditions. Three different initial H_2O amounts of 0.5, 1, and 2 wt.% were considered together with 1,000 ppm of CO_2, 2,000 ppm of S and 2,000 ppm of Cl typical for Etnean magmas (Spilliaert *et al.*, 2006; Collins *et al.* 2009; Lanzafame *et al.*, 2013). Results indicate that 0.5, 1, and 2 wt.% H_2O start to exsolve at about 10, 20, and 55 MPa, respectively (Fig. 12).

Additionally, bubbles attain the range of 10-30 vol.% measured in this study at about 5, 11, and 30 MPa (Tables 1 and 2, Fig. 12).

A further computation focused on the *liquidus* temperature considering 0, 1, and 2 wt.% H_2O up to the limit pressures to retain water dissolved in the magma at fO_2 of NNO+1. These set of numerical results are compared with the initial T of crystallization of plg and cpx (Mollo *et al.*, 2011). Under anhydrous conditions, the liquidus temperature corresponds to 1,190-1,200 °C, whereas with 1 and 2 wt.% H_2O the liquidus temperature decreases to 1,130 and 1,075 °C, respectively. However, the computation with 2 wt.% H_2O does not match at all with the initial T of plg and cpx crystallization (Fig. 12). The computation with 1 wt.% H_2O produces up to 30 vol.% at 10-16 MPa, corresponding to depth of 350-600 m for 2,500 kg/m^3 density, below the dyke magma pressure level of 2-9 MPa. Also, 1 wt.% H_2O originally dissolved in magma means that 0.25-0.5 wt.% H_2O exsolved at pressure ≥ 2-9 MPa. Thus, the shallow magma contained only 0.5-0.75 wt.% H_2O (Fig. 12), in agreement with the water concentration estimated to be in equilibrium with the crystals at the onset of plg and cpx crystallization (Mollo *et al.*, 2011). Up to 30 vol.% of bubbles formed before that the magma attained pressures of 2-9 MPa where H_2O exsolved (Fig. 12). In turn, transient to turbulent regimes recorded by most bubbles occurred when the magma was at pressures comprised between 9 and 16 MPa (Fig. 12). A non-laminar dynamic flow probably took place also at P < 16 MPa, but it is not detectable due to the lack of phases at $P \geq 16$ MPa. The computation with 0.5 wt.% H_2O produces similar results but at pressures lower than those determined using 1 wt.% H_2O.

When the magma attained a pressure level between 2-9 MPa, 1 wt.% H_2O further exsolved (Fig. 12) accompanied by temperature decrease due to the contact with the cold wall rock. Both decompression and cooling determined a rapid and massive crystallization with formation of new cpx and plg nuclei or by overgrown on early-formed crystals by attachment processes (Iezzi *et al.*, 2008, 2011 and 2014). All these aspects favoured abrupt increase of crystals in magma, decelerating

or even arresting the flowage. The last step of crystallization occurred at $T < 1{,}100$ °C as recorded by plg and cpx crystal rims (Mollo *et al.*, 2011).

In order to evaluate the rheological conditions plausible for dyke solidification and fluid-dynamic, the density change of magma has been simulated in a closed-system as a function of P, 1 wt.% H_2O, 950-1,150 °C, and 0-40 wt.% plg and 15 wt.% cpx. The solubility model of Papale *et al.*, (2006) was used to calculate wt.% and mol.% of H_2O dissolved and exsolved, whereas the density of magma was calculated by Conflow (Mastin, 2002). All these data were used as input parameters for the ideal gas law:

$$V = R \times \mathrm{n} \times T / P,$$

where V is volume (m^3), n is mole (mol.%) and R is the universal gas constant (see the supplementary Excel spreadsheets). At 5.5 and 6.5 MPa, the gas phase is 10-30 vol.% resembling to the total amount of bubbles (Figs. 12 and 13). This narrow range of P corresponds also to a rapid change in density roughly comprised between 1,800 and 2,400 kg/m^3. It is worth noting that at $P <$ 10 MPa the amount of gas is low or absent and the density of the magmatic suspension slightly changes of about 150 kg/m^3 (the density of plg, cpx, and melt is 2,700, 3,250, and 2,600 kg/m^3, respectively). In general, dykes intruding with a low overpressure can ascend according to a density contrast between magma and country-rocks (Carrigan, 2000; Jaupart, 2000; Gonnerman & Taisne, 2015). In the present case, if the magma was injected with a low overpressure, its upraising was possible only for a wall rock density > 2,400 kg/m^3 (Fig. 13).

The retrieved magma densities have been used for the calculation of the Reynolds numbers, trough the equation:

$$Re = \rho \times d \times v / \eta,$$

where ρ is density of the magma between 1,800 (30 vol.% bubbles) and 2,500 (free of crystals and with a few bubbles) kg/m^3, d is the dyke width, v is the average ascent velocity, and η is the magma viscosity. The viscosity of the melt was calculated by the equation of Giordano *et al.* (2008) at 0.5 and 1 wt.% H_2O and 1,000-1,200 °C, while the effect of crystals on viscosity has been modelled

using data from Vona *et al.* (2011), considering crystals with 3:1 aspect ratio and 0.1 s^{-1} strain rate. The progressive differentiation of the residual melt as a function of crystals and bubbles has not been considered, being this strategy clearly conservative due to the fact that melt viscosity increases with increasing SiO_2 of the melt (Gonnerman & Manga, 2012; Mangan *et al.*, 2014). Viscosity paths are very similar, with only a weak downward shifting at 0.5 wt.% H_2O (Fig. 14). Overall, the viscosity increases of about two orders of magnitude when the crystal content increases from 0 to 40 vol.%, but the most important changes are observed for crystallization up to 50 vol.% (Fig. 14).

These viscosities values were translated to Re numbers at 1,800 and 2,500 kg/m^3, considering five different ascent velocities of 0.1, 1, 2.5, 5, and 10 m/s (Fig. 14), reproducing the range estimated for Etnean magmas (Mollo *et al.*, 2015b). Critical Re numbers were set at 1,000 and 2,000 for shifting from laminar-to-transitional and transitional-to-turbulent regimes, respectively (Huppert & Sparks, 1985; Emerman & Turcotte, 1986, Spence & Turcotte, 1990). Results show that, at T < 1,200 °C and density of 1,800 kg/m^3, an ascent velocity > 2.5 m/s is sufficient to pierce the transitional field when the crystal content is < 10 vol.% and H_2O is 0.5-1 wt.% (Fig. 14). At these conditions, the turbulent regime is triggered for an ascent velocity > 5 m/s (Fig. 14). At lower values, non-laminar regimes are produced when the temperature decreases and the crystal content increases (Figs. 13 and 14). These numerical results rationally support the transient and/or turbulent regimes deduced by the textural and fabric characteristics of bubbles (Tab. 3 and Figs. 4, 4S, 6 and 9).

CONCLUSIONS

In the case of an Etnean dyke, the comparison between 2D and 3D data on bubbles indicates that common 2D textures give confident quantification of the amount, number per area, size, and shape of bubbles, whereas the bubble connectivity and orientation remain unreliable using a two-dimensional approach. The dyke emplacement occurred at P-T-fO_2-H_2O values close to the *liquidus*

condition of magma. Under such circumstances, transition to turbulent regimes determined a more uniform distribution of the ascent velocity and a random variation of the strain rate. Indeed, volcanic rocks showing mingled textural features can not be inevitably consider to result from mixture of two magmas.dyke

Acknowledgements

The 2D data reported in this study were first collected and treated during the Master thesis of F.L. at the University G. d'Annunzio. This work was possible thanks to the support of the following institutions and programs: Università G. d'Annunzio - "Fondi Ateneo" and PRIN project "Experimental determination of the glass-forming ability, nucleation and crystallization of natural silicate melts" awarded to Gianluca Iezzi.

References

Acocella, V. & Neri, M. (2009). Dyke propagation in volcanic edifices: Overview and possible developments. *Tectonophysics* **471**, 67-77.

Álvarez-Valero, A.M., Okumura, S., Arzilli, F., Borrajo, J., Recio, C., Ban, M., Gonzalo, J.C., Benítez, J.,M., Douglas, M., Sasaki, O., Franco, P., Gómez-Barreiro, J., Carnicero, A. (2016). Tracking bubble evolution inside a silicic dyke. *Lithos* **262**, 668-676.

Al-Raoush, R. & Papadopoulos, A., 2010. Representative elementary volume analysis of porous media using X-ray computed tomography. *Powder technology* **200**, 69-77.

Andersson, M., Almqvist, B.S.G., Burchardt, S., Troll, V.R., Malehmir, A., Snowball I. & Kübler, L. (2016) Magma transport in sheet intrusions of the Alnö carbonatite complex, central Sweden. *Scientific Reports* **6**, 27635, doi: 10.1038/srep27635.

Aubourg, C., Tshoso, G. Le Gall, B., Bertrand, C. , Tiercelin, J.J., Kampunzu, A.B., Dyment, J. & Modisi, M. (2008). Magma flow revealed by magnetic fabric in the Okavango giant

dyke swarm, Karoo igneous province, northern Botswana. *Journal of Volcanology and Geothermal Research* **170**, 247–261.

Baker, D.R., Brun, F., O'Shaughnessy, C., Mancini, L., Fife, J.L. & Rivers, M. (2012) A four-dimensional X-ray tomographic microscopy study of bubble growth in basaltic foam. *Nature Communications* **3**, 1135, doi:10.1038/ncomms2134.

Bascou, J., Camps, P. & Dautria, J.M. (2005). Magnetic versus crystallographic fabrics in a basaltic lava flow. *Journal of Volcanology and Geothermal Research* **145**, 119– 135.

Benn, D.I. (1994) Fabric shape and the interpretation of sedimentary fabric data. *Journal of Sedimentary Research*, **A64**, 4, 910-915.

Bjarne, S., Almqvist, G., Bosshard, S.A., Hirt, A.M., Mattsson, H.B. & Hetényi, G. (2012). Internal flow structures in columnar jointed basalt from Hrepphólar, Iceland: II. Magnetic anisotropy and rock magnetic properties. *Bulletin of Volcanology* **74**, 1667–168.

Branca, S., Coltelli, M., De Beni, E. & Wijbrans, J. (2008). Geological evolution of Mount Etna volcano (Italy) from earliest products until the first central volcanism (between 500 and 100 ka ago) inferred from geochronological and stratigraphic data. *International Journal of Earth Sciences* **97**, 135-152.

Bruce, P.M. & Huppert H.E. (1990). *Solidification and melting along dykes by the laminar flow of basaltic magma*. In: Ryan, P. (ed.) *Magma Tranrport and Storage*. John Wiley and Sons, 87-102.

Brun, F., Mancini, L., Kasae, P., Favretto, S., Dreossi, D. & Tromba, G. (2010). Pore3D: a software library for quantitative analysis of porous media. *Nuclear Instruments* and *Methods* in Physics Research A **615**, 3, 326-332.

Brun, F., Kourousias, G., Dreossi, D., Mancini, L. & Tromba, G. (2011). A comparative evaluation of ring artifacts reduction filters for X-Ray computed microtomography images. *Proceedings of the International Conference on Image Processing*, ICP **6116535**, 405-408.

Campbell, I. & Schenk, E.T. (1950). Camptonite dykes near Boulder Dam, Arizona. *American Mineralogist* **35**, 671-692.

Callot, J.P, Geoffroy, L., Aubourg, C., Pozzi, J.P. & Mege, D., (2001). Magma flow directions of shallow dykes from the East Greenland volcanic margin inferred from magnetic fabric studies. Tectonophysics **335**, 313–329.

Calvari, S., Groppelli, G. & Pasquarè, G. (1994). Preliminary geological data on the south-western wall of the Valle del Bove, Mt. Etna, Sicily. *Acta Vulcanologica* **5**, 15-30.

Cañón-Tapia, E. & Chávez-Álvarez, M.J. (2004) Theoretical aspects of particle movement in flowing magma: implications for the anisotropy of magnetic susceptibility of dykes. *Geological Society of London, Special Publications* **238**, 227-249, doi:10.1144/GSL.SP.2004.238.01.15.

Cañón-Tapia, E. & Herrero-Bervera, E. (2009). Sampling strategies and the anisotropy of magnetic susceptibility of dykes. *Tectonophysics* **466**, 3–17.

Carrigan, C.R., Schubert, G. & Eichelbergr, J.C. (1992). Thermal and Dynamical Regimes of Single- and Two-Phase Magmatic Flow in Dykes. *Journal of Geophysical Research* **97**, B12, 17377-17392.

Carrigan, C. R. (2000). Plumbing systems. In: Sigurdsson, H., Houghton, B., Rymer, H., Stix, J. & McNutt, S. (eds.) *The Encyclopedia of Volcanoes 1st edition*, Academic Press, 219-235.

Cashman, K.V. (1992). Textural constraints on the kinetics of crystallization of igneous rocks. *Reviews in Mineralogy and Geochemistry* **24**, 1, 259-314.

Catalano, S., Torrisi, S. & Ferlito, C. (2004). The relationship between Late Quaternary deformation and volcanism of Mt. Etna (eastern Sicily): new evidences from the sedimentary substratum in the Catania region. *Journal of Volcanology and Geothermal Research* **132**, 311-314.

Chistyakova, S.Y & Latypov, R.M. (2009). Two independent processes responsible for compositional zonation in mafic dykes of the Åland-Åboland Dyke Swarm, Kestiö Island, SW Finland. *Lithos* **112**, 382–396.

Clemente, C.S., Amoròs, E.B. & Crespo, M.G. (2007). Dyke intrusion under shear stress: Effects on magnetic and vesicle fabrics in dykes from rift zones of Tenerife (Canary Islands). *Journal of Structural Geology* **29**, 1931-1942

Collins, S.J., Pyle, D.M. & Maclennan, J. (2009). Melt inclusions track pre-eruption storage and dehydratation of magmas at Etna. *Geology* **6**, 571–574.

Coltelli, M., Garduño, V.H., Neri, M., Pasquarè, G. & Pompilio, M. (1994). Geology of the northern wall of the Valle del Bove, Mt. Etna (Sicily). *Acta Vulcanologica* **5**, 55-68.

Corsaro, R.A., Métrich, N., Allard, P., Andronico, D., Miracglia, L. & Fourmentraux, C. (2009).The 1974 flank eruption of Mount Etna: An archetype for deep dyke-fed eruptions at basaltic volcanoes and a milestone in Etna's recent history. *Journal of Geophysical Research Solid Earth* **114**, B7, doi: 10.1029/2008JB006013

Cristofolini, R., Lentini, F., Patanè, G. & Rasà, R. (1979). Integrazione di dati geologici, geofisici e petrologici per la stesura di un profilo crostale in corrispondenza dell'Etna. Bollettino della Società Geologica Italinana **98**, 239-247.

Daniels, K.A., Kavanagh, J.L., Menand, T. & Sparks, R.S.J. (2012). The shapes of dykes: Evidence for the influence of cooling and inelastic deformation. *Bulletin of the Geological Society of America* **124**, 1102-1112.

Daniels, K.A., Bastow, I.D., Keir, D., Sparks, R.S.J. & Menand, T. (2014). Thermal models of dyke intrusion during development of continent-ocean transition. *Earth and Planetary Science Letters*, **385**, 145-153.

De Beni, E., Wijbrans, J.R., Branca, S., Coltelli, M. & Groppelli, G. (2005). New results of Ar-40/Ar-39 dating constrain the timing of transition from fissure-type to central volcanism at Mount Etna (Italy). *Terra Nova* **17**, 292-298.

Delaney P.T., Pollard D.D., Ziony J.I. & McKee E.H. (1986). Field relations between dykes and joints: Emplacement processes and paleostress analysis. *Journal of Geophysical Research* **91**, 4920-4938.

Del Gaudio, P., Mollo, S., Ventura, G., Iezzi , G., Taddeucci, J. & Cavallo A. (2010). Cooling rate-induced differentiation in anhydrous and hydrous basalts at 500 MPa: Implications for the storage and transport of magmas in dykes. *Chemical Geology* **270**, 164-178.

D'Orazio, M., Tonarini, S., Innocenti, F. & Pompilio, M. (1997). Northern Valle del Bove volcanic succession (Mt. Etna, Sicily): petrography, geochemistry and Sr-Nd isotope data. *Acta Vulcanologica* **9**, 73-86.

Emerman, S.H. & Turcotte, D.L (1986). Transport of magma and hydrothermal solutions by laminar and turbulent fluid fracture. *Physics of the Earth and Pidnetary interiors*, **41,** 249-259.

Ernst, R.E. & Baragart, W.R.A. (1992). Evidence from magnetic fabric for the flow pattern of magma in the Mackenzie giant radiating dyke swarm. *Nature* **356**, 511-513, doi:10.1038/356511a0.

Eriksson, P.I., Riishuus, M.S., Sigmundsson, F. & Elming, S.A. (2011). Magma flow directions inferred from field evidence and magnetic fabric studies of the Streitishvarf composite dyke in east Iceland. *Journal of Volcanology and Geothermal Research* **206**, 30–45.

Feldkamp, L.A., Davis, L.C. & Kress, J.W. (1984). Practical cone-beam algorithm. *Journal of the Optical Society of America* **A1**, 612-619.

Femenias, O., Diot, H., Berza, T., Gauffriau, A. & Demaiffe, D. (2004). Asymmetrical to symmetrical magnetic fabric of dykes: Paleo-flow orientations and Paleo-stresses recorded on feeder-bodies from the Motru Dyke Swarm (Romania). *Journal of Structural Geology* **26**, 1401-1418.

Ferlito, C. & Cristofolini, R. (1989). Geologia dell'area sommitale dell'Etna. *Bollettino dell'Accademia Gioenia di Scienze Naturali di Catania* **22**, 357-380.

Ferlito, C. & Lanzafame, G. (2010). The role of supercritical fluids in the potassium enrichment of magmas at Mount Etna volcano (Italy). *Lithos* **119**, 642-650.

Ferlito, C. & Nicotra, E. (2010). The dyke swarm of Mount Calanna (Etna, Italy): an example of the uppermost portion of a volcanic plumbing system. Bulletin of Volcanology **72**, 10, 1191-1207.

Ferlito, C., Coltorti, M., Lanzafame, G. & Giacomoni, P.P. (2014). The volatile flushing triggers eruptions at open conduit volcanoes: Evidence from Mount Etna volcano (Italy). *Lithos*, **184**, 447- 455, doi:10.1016/j.lithos.2013.10.030.

Fiege, A., Vetere, F., Iezzi, G., Simon, A. & Holt, F. (2015). The roles of decompression rate and volatiles (H2O + Cl ± CO_2 ± S) on crystallization in (trachy-) basaltic magma *Chemical Geol*ogy **411**, 310-322.

Giacomoni, P.P., Ferlito, C., Coltorti, M., Bonadiman, C. & Lanzafame, G. (2014). Plagioclase as Archive of Magma Ascent Dynamics on "Open Conduit" Volcanoes: The 2001-2006 Eruptive Period at Mt. Etna. *Earth-Science Reviews* **138**, 371–393.

Galindo, I. & Gudmundsson, A. (2012). Basaltic feeder dykes in rift zones: geometry, emplacement, and effusion rates. *Natural Hazards Earth Systems Sciences*, **12**, 3683-3700.

Geshi N. & Neri M. (2011). Dynamic feeder dyke systems in basaltic volcanoes: the exceptional example of the 1809 Etna eruption (Italy). *Frontiers in Earth Science* **2**, 1-11.

Gillot, P.Y., Kieffer, G. & Romano, R. (1994). The evolution of Mount Etna in the light of potassium-argon dating. *Acta Vulcanologica* **5**, 81-87.

Giordano, D., Russell, J.K. & Dingwell, D.B. (2008). Viscosity of magmatic liquids: a model. *Earth and Planetary Science Letters* **271**, 123–134

Gitman, I. M., Askes, H. & Sluys, L.J., (2007), Representative volume: Existence and size determination. *Engineering Fracture Mechanics*, **74**(16), 2518-2534.

Gonnermann, H.M. & Manga, M. (2012). Dynamics of magma ascent in the volcanic conduit. In: Fagents, S.A., Gregg, T.K.P. & Lopes, R.M.C. (Eds.) *Modeling Volcanic Processes: The Physics and Mathematics of Volcanism*, Cambridge University Press.

Gonnermann, H. & Taisne, B. (2015). Magma Transport in Dykes. In: Sigurdsson H., Houghton, B., McNutt, S., Rymer, H., & Stix, J. (eds.) *The Encyclopedia of Volcanoes*, 2nd edition, San Diego, CA, 215-224.

Gray, N.H. (1970). Crystal growth and nucleation in two large diabase dykes. *Canadian Journal of Earth Sciences* **7**, 366-375.

Gray, N.H. (1978). Crystal growth and nucleation in flash-injected diabase dykes. *Canadian Journal of Earth Sciences* **15**, 1904-1923.

Gudmundsson, A. (2006). How local stresses control magma-chamber ruptures, dyke injections, and eruptions in composite volcanoes. *Earth-Science Reviews* **79**, 1-31.

Gudmundsson, A., Marinoni, L.B. & Marti, J. (1999). Injection and arrest of gykes: implications for volcanic hazards. *Journal of Volcanology and Geothermal Research* **88**, 1-13.

Hammer, J.E. (2008). Experimental studies of the kinetics and energetics of magma crystallization. In: Putirka, K.D. & Tepley, F.J. (eds.) Minerals, Inclusions and Volcanic Processes. *Review in Mineralogy and Geochemistry* **69**, 9-59.

Hastie, W.H., Aubourg, C. & Watkeys, M.K. (2011). When an 'inverse' fabric is not inverse: an integrated AMS-SPO study in MORB-like dykes. *Terra Nova* **23**, 49–55.

Hastie, W.H., Watkeys, M.K. & Aubourg, C. (2013). Characterisation of grain-size, shape and orientation of plagioclase in the Rooi Rand dyke swarm, South Africa. *Tectonophysics* **583**, 145–157.

Herrero-Bervera, E., Walker, G.P.L., Cañon-Tapia, E. & Garcia, M.O. (2001). Magnetic fabric and inferred flow direction of dykes, conesheets and sill swarms, Isle of Skye, Scotland. *Journal of Volcanology and Geothermal Research* **106**, 195-210.

Higgins, M.D., (2006). Quantitative textural measurements. In: Cambridge University Press (ed.), *Igneous and Metamorfic Petrology*.

Hildebrand, T. & Rüegsegger, P., (1997). A new method for the model-independent assessment of thickness in three-dimensional images. *Journal of Microscopy* **185,** 67–75.

Holmes, A. & Iarwood, H.F., (1929). The tholeiite dykes of the north of England. *Mineralogical Magazine* **22**, 1-52.

Howard, M.P. (1980). The analysis of flow profiles in a basaltic dyke using strained in a basaltic dyke using strained vesicles. *Journal of the Geological Society* **137**, 605-615.

Huppert, H.E. & Sparks, R.S.J. (1985). Cooling and contamination of mafic and ultramafic magmas during ascent through continental crust. *Earth and Planetary Science Letters* **74**, 371-386.

Iezzi, G. & Ventura, G. (2002). Crystal fabric evolution in lava flows: results from numerical simulations. *Earth and Planetary Science Letters* **200**, 33-46.

Iezzi, G., Mollo, S., Ventura, G., Cavallo, A. & Romano, C. (2008). Experimental solidification of anhydrous latitic and trachytic melts at different cooling rates: the role of nucleation kinetics. *Chemical Geology* **253**, 91-101.

Iezzi G., Mollo S., Torresi G., Ventura G., Cavallo A. & Scarlato P. (2011). Experimental solidification of an andesitic melt by cooling. *Chemical Geology* **283**, 261-273.

Iezzi G., Mollo S., Shahini E., Cavallo A. & Scarlato P. (2014). The cooling kinetics of plagioclase feldspar as revealed by electron-microprobe mapping. *American Mineralogist* **99**, 898-907.

Ikeda, Y. (1977). Grain size of plagioclase of the basaltic andesite dykes, Iritono, central Abukuma plateau. *Canadian Journal of Earth Sciences* **14**, 1860-1866.

Jaupart, C. (2000). Magma ascent at shallow levels. In: Sigurdsson, H., Houghton, B., Rymer, H., Stix, J. & McNutt, S. (eds.) *The Encyclopedia of Volcanoes 1st edition*, Academic Press, 237-245.

Kille, I.C., Thompson, R.N., Morrison, M.A. & Thompson, R.F., (1986). Field evidence for turbulence during flow of basalt magma through conduits from southwest Mull. *Geological Magazine* **123,** 693-697.

Komar, P.D. (1972). Flow differentiation in igneous dykes and sills: profiles of velocity and phenocryst concentration. *Geological Society of America Bulletin* **83**, 3443-3448.

Komar, P.D. (1976). Phenocryst interactions and the velocity profile of magma flowing through dykes or sills. *Geological Society of America Bulletin* **87**, 1336-1342.

Lanzafame, G. & Vestch, P. (1985). Les dykes de la Valle del Bove (Etna, Sicile) et le champ de constraints régionales. *Revue de Géographie Physique et de Gèologie Dynamique* **26**, 147-156.

Lanzafame, G., Mollo, S., Iezzi, G., Ferlito, C. & Ventura, G. (2013). Unraveling the solidification path of *pahoehoe* "cicirara" lava from Mount Etna volcano. *Bulletin of Volcanology* **75**, 703-719.

Lee, T.C., Kashyap, R.L. & Chu, C.N. (1994). Building skeleton models via 3D medial surface axis thinning algorithms. *CVGIP: Graphical Models and Image Proceedings* **56**, 6, 462-478, doi: 10.1006/cgip.1994.1042.

Lindquist, W.B. & Lee, S.M. (1996). Medial axis analysis of void structure in three-dimensional tomographic images of porous media. *Journal of Geophysical Research* **101**, B4, 8297-8310.

Lister, J.R. & Kerr, R.C., (1991). Fluid mechanical models of crack propagation and their application to magma transport in dykes. *Journal of Geophysical Research* **96**, 10049-10077.

Maccaferri, F., Bonafede, M. & Rivalta, E. (2011). A quantitative study of the mechanisms governing dyke propagation, dyke arrest and sill formation. *Journal of Volcanology and Geothermal Research* **208**, 39-50.

Maimon O., Lyakhovsky, V., Melnik, O. & Navon, O. (2012). The propagation of a dyke driven by gas-saturated magma. *Geophysical Journal International* **189**, 956-966.

Mangan, M.T., Cashman, K.V. & Swanson, D.A. (2014). The Dynamics of Hawaiian-Style Eruptions: A Century of Study. In: Poland, M.P., Takahashi, T.J. & Landowski C.M. (eds.) *Characteristics of Hawaiian Volcanoes*, U.S. Geological Survey Professional Paper 1801.

Mancini, L., Dreossi, D., Fava, C., Sodini, N., Tromba, G., Faretto, S. & Montanari, F. (2007). TOMOLAB: The new X-ray microtomography facility @ ELETTRA. *Elettra Highlights* 2006-2007.

Mastin, L. G. (2002). Insights into volcanic conduit flow from an open-source numerical model. *Geochemistry Geophysics Geosystems* **3**, 1-18, doi:10.1029/2001GC000192.

McGuire, W.J. (1982). Evolution of the Etna volcano: information from the southern wall of the Valle del Bove caldera. Journal of Volcanology and Geothermal Research **13**, 241-271.

McLeod, P. & Tait, S. (1999). The growth of dykes from magma chambers. *Journal of Volcanology and Geothermal Research* **92**, 231-245.

Menand, T. & Tait, S.R. (2001). A phenomenological model for precursor volcanic eruptions. *Nature* **411**, 678-680.

Mollo, S., Lanzafame, G., Masotta, M., Iezzi, G., Ferlito, C. & Scarlato, P. (2011). Cooling history of a dyke as revealed by mineral chemistry: a case study from Mt. Etna volcano. *Chemical Geology* **288**, 39-52.

Mollo, S., Misiti, V., Scarlato, P. & Soligo, M. (2012). The role of cooling rate in the origin of high temperature phases at the chilled margin of magmatic intrusions. *Chemical Geology* **322-323**, 28-46, doi:10.1016/j.chemgeo.2012.05.029.

Mollo S., Putirka K., Iezzi G. & Scarlato P. (2013). The control of cooling rate on titanomagnetite composition: implications for a geospeedometry model applicable to alkaline rocks from Mt. Etna volcano Contrib Mineral Petrol (2013) 165:457–475. DOI 10.1007/s00410-012-0817-6.

Mollo S., Giacomoni P.P.,. Coltorti M., Ferlito C, Iezzi G., Scarlato P., (2015a). Reconstruction of magmatic variables governing recent Etnean eruptions: constraints from mineral chemistry and P-T-fO2-H2O modelling, Lithos, 212-215, 311-320, 10.1016/j.lithos.2014.11.020.

Mollo S., Giacomoni P.P., Andronico D., Scarlato P., (2015b). Clinopyroxene and titanomagnetite cation redistributions at Mt. Etna volcano (Sicily, Italy): Footprints of the final

solidification history of lava fountains and lava flows, Chemical Geology, 406, 45-54, http://dx.doi.org/10.1016/j.chemgeo.2015.04.017.

Monaco, C., Tapponier, P., Tortorici, L. & Gillot, P.Y. (1997). Late Quaternary slips rates on the Acireale-Piedimonte normal faults and tectonic origin of Mt. Etna (Sicily). *Earth and Planet Science Letter*s **147**, 125-139.

Monaco, C., Catalano, S., Cocina, O., De Guidi, G., Ferlito, C., Gresta, S., Musumeci, C. & Tortorici, L. (2005) Tectonic control on the eruptive dynamics at Mt. Etna volcano (Sicily) during the 2001 and 2002-2003 eruptions. *Journal of Volcanology and Geothermal Research* **144**, 211-233.

Monaco, C., De Guidi, G. & Ferlito C. (2010). The morphotectonic map of Mt. Etna. Bollettino della Società Geologica Italiana **129**, 3, 408-428.

Nkono, C., Féménias, O., Diot, H., Berza, T. & Demaiffe, D. (2006). Flowage differentiation in an andesitic dyke of the Motru Dyke Swarm (Southern Carpathians, Romania) inferred from AMS, CSD and geochemistry. *Journal of Volcanology and Geothermal Research* **154**, 201- 221.

Odgaard, A. & Gundersen, H.I.G. (1993). Quantification of connectivity in cancellous bone, with special emphasis on 3D reconstructions. *Bone* **14**, 173-182, doi: 10.1016/8756-3282(93)90245-6.

Ohser, J. & Mücklich, F. (2000). Statistical Analysis of Microstructure in Material Science. In: Barnett, V. (ed.) *Statistics in Practice*. John Wiley & Sons, West Sussex, England, 381 p.

Otsu, N. (1979). A threshold selection method from gray-level histograms. *IEEE Transactions on Systems,Man and Cybernetics* **9**, 62-6.

Papale, P., Moretti, R. & Barbato, D. (2006). The compositional dependence of the saturation surface of $H_2O + CO_2$ fluids in silicate melts. *Chemical Geology* **229**, 78-95.

Perinelli C., Mollo S., Gaeta M., De Cristofaro S. P., Palladino D. M., Armienti P., Scarlato P. & Putirka, K.D. (2016). An improved clinopyroxene-based hygrometer for Etnean magmas and

implications for eruption triggering mechanisms. *American Mineralogist* **101**, 2774–2777, doi: 10.2138/am-2016-5916.

Pinel, V. & Jaupart, C. (2004). Magma storage and horizontal dyke injection beneath a volcanic edifice. *Earth and Planetary Science Letters* **221**, 245-262.

Philpotts, A.R. & Philpotts, D.E. (2007). Upward and downward flow in a camptonite dyke as recorded by deformed vesicles and the anisotropy of magnetic susceptibility (AMS). *Journal of Volcanology and Geothermal Research* **161**, 81–94.

Polacci, M., Baker, D.R., Mancini, L., Favretto, S. & Hill, R.J. (2009). Vesiculation in magmas from Stromboli and implications for normal Strombolian activity and paroxysmal explosions in basaltic systems. *Journal of Geophysical Research Solid Earth*, **114**, B01206.

Poland, M.P., Fink, J. H. & Tauxe, L. (2004). Patterns of magma flow in segmented silicic dykes at Summer Coon volcano, Colorado: AMS and thin section analysis, Earth Planet. Sci. Lett., 219(1 – 2), 155 – 169, doi:10.1016/S0012-821X(03)00706-4.

Pollard, D.D. (1973). Derivation and evaluation of a mechanical model for sheet intrusions. *Tectonophysics* **19**, 233-269.

Pollard, D. D. (1976). On the form and stability of open hydraulic fractures in the Earth's crust, *Geophysical Research Letters* **3**, 513-516.

Pollard, D. D., (1987). Elementary fracture mechanics applied to the structural interpretation of dykes. *Geological Association of Canada Special Papers* **34**, 5-24.

PORE3D - A software library for quantitative analysis on porous media: 2009, http://www.elettra.eu/pore3D.

Queneau, A.L. (1902). Size of grain in igneous rocks in relation to the distance from the cooling wall. *School of Mines Quarterly New York* **23**, 181-195.

Quinn, A. W. (1943). Settling of heavy minerals in a granodiorite dyke at Bradford, Rhode Island. *American Mineralogist* **28**, 272-281.

Rivalta, E., B. Taisne, A. P. Bunger & Katz, R.F. (2015). A review of mechanical models of dyke propagation: Schools of thought, results and future directions. *Tectonophysics* **638**, 1-42.

Romano, R. (1982). Succession of the volcanic activity in the Etnean area. *Memorie della Società Geologica Italiana* **23**, 27-48.

Rubin, A.M. (1995). Propagation of magma-filled cracks. *Annual Review of Earth and Planetary Science* **23**, 287-336.

Russ, J.C. & DeHoff, R.T. (1986). *Practical Stereology*, New York, Plenum Press, 381 p.

Scarlato, P., Mollo, S., Blundy, J.D., Iezzi, G. & Tiepolo, M. (2014). The role of natural solidification paths on REE partitioning between clinopyroxene and melt. *Bulletin of Volcanology* **76**, 810.

Serra, J. (1982). *Image Analysis and Mathematical Morphology.* Academic Press, London, 610 p.

Shelley, D. (1985). Determining paleo-flow directions from groundmass fabrics in the Lyttelton radial dykes, New Zeland. *Journal of Volcanology and Geothermal Research* **25**, 69-79.

Sigurdsson, H. (2000). The History of Volcanology In: Sigurdsson, H. (Ed.), Sigurdsson, H., Houghton, B., Rymer, H., Stix, J. & McNutt, S. (eds.) *The Encyclopedia of Volcanoes 1st edition*, Academic Press, New York, 15-37.

Sijbers, J., Postnov, A., (2004). Reduction of ring artifacts in high resolution micro-CT reconstructions. Physics in Medicine and Biology **49**, 247-253.

Spence D.A. & Turcotte D.L., (1990). Buoyancy-Driven Magma Fracture' A Mechanism for Ascent Through the Lithosphere and the Emplacement of Diamonds. *Journal of Geophysical Research* **95**, B4, 5133-5139.

Spera, F.J. (1980). Aspects of magma transport. In: Hargraves, R.B. (Ed.), *Physics of Magmatic Processes*. Princeton University Press, 232-265.

Spilliaert, N., Allard, P., Métrich, N. & Sobolev, A.V. (2006). Melt inclusion record of the conditions of ascent, degassing, and extrusion of volatile-rich alkali basalt during the powerful 2002 flank eruption of Mount Etna (Italy). Jornal of Geophysical Research 111, B04203.

Taisne B. & Jaupart C. (2009). Dyke propagation through layered rocks. *Journal of Geophysical Research* **114**, B09203.

Taisne, B., Tait, S. & Jaupart, C. (2011). Conditions for the arrest of a vertical propagating dyke. *Bulletin of Volcanology* **73**, 191-204.

Tanguy, J.C., Condomines, M. & Kieffer, G. (1997). Evolution of Mount Etna: constraints on the present feeling system and eruptive mechanism. *Journal of Volcanology and Geothermal Research* **75**, 221-250.

Tanguy, J.C., Condomines, M., Le Goff, M., Chillemi, V., La Delfa, S. & Patanè, G. (2007). Mount Etna Eruption of the last 2, 750 years: revised chronology and location through archeomagnetic and 226Ra-230Th dating. *Bulletin of Volcanology* **70**, 55-83.

Tartese, R. & Boulvais, P. (2010). Differentiation of peraluminous leucogranites “en route” to the surface. *Lithos* **114**, 353–368.

Teall, J.J.H. (1884). Petrological notes on some north-of-England dykes. *The Quarterly Journal of the Geological Society of London* **40**, 209-247.

TOMOLAB—X-ray CT laboratory, 2010, www.elettra.trieste.it/Labs/TOMOLAB.

Vetere, F., Iezzi, G., Behrens, H., Cavallo, A., Misiti, V., Dietrich, M., Knipping, J., Ventura, G. & Mollo, S. (2013). Intrinsic solidification behaviour of basaltic to rhyolitic melts: A cooling rate experimental study. *Chemical Geology* **354**, 233-242.

Vetere, F., Mollo, S., Giacomoni , P.P., Iezzi, G., Coltorti, M., Ferlito, C., Holtz, F., Perugini, D. & Scarlato, P. (2015a). Experimental constraints on the origin of pahoehoe “cicirara” lavas at Mt. Etna Volcano (Sicily, Italy). *Bulletin of Volcanology* **77**, 44, doi: 10.1007/s00445-015-0931-1

Vetere F., Iezzi G., Behrens H., Holtz F., Ventura G., Misiti V., Cavallo A., Mollo S., Dietrich M. (2015b). Glass forming ability and crystallization behaviour of sub-alkaline silicate melts. *Earth-Science Reviews* **150**: 25-44.

Vona, A., Romano, C., Dingwell, D.B. & Giordano, D. (2011). The rheology of crystal-bearing basaltic magmas from Stromboli and Etna. *Geochimica et Cosmochimica Acta* **75**, 3214-3236.

Wada, Y. (1992). Magma flow directions inferred from preferred orientations of phenocrysts in a composite feeder dyke, Miyake-Jima, Japan. *Journal of Volcanology and Geothermal Research* **49**, 119-126.

Walter, J.M., Iezzi, G., Albertini, G., Gunter, M.E., Piochi, M., Ventura, G., Jansen, E. & Fiori, F. (2013). Enhanced crystal fabric analysis of a lava flow sample by neutron texture diffraction: A case study from the Castello d'Ischia dome. *Geochemistry, Gophisics, Geosystems* **14**, 179–196, doi:10.1029/2012GC004431.

Weickert, J. (1998). *Anisotropic diffusion in image processing*. Teubner, Stuttgart, Germany.

Whitam, F.,Blundy, J. & Kohn, S.C. (2012). SolEx: Amodel for mixed COHSCl-volatile solubilities and exsolved gas compositions in basalt. *Computer & Geosciences* **45**, 87-97.

Winkler, H.G.F. (1948). Crystallization of basaltic magma as recorded by variation of crystal-size in dykes. *Mineralogical Magazine*, **28**, 557-554.

Yamato, P., Tartèse, R., Duretz, T. & May, D.A. (2012). Numerical modelling of magma transport in dykes. *Tectonophysics* **526**, 97-109.

Yamato P., T. Duretz , D.A.May , R. Tartèse Quantifying magma segregation in dykes Tectonophysics 660 (2015) 132-147

Zandomeneghi, D., Voltolini, M., Mancini, L., Brun, F., Dreossi, D. & Polacci, M. (2010). Quantitative analysis of X-ray microtomography images of geomaterials: Application to volcanic rocks. *Geosphere* **6**, 793-804, doi:10.1130/GES00561.1.

Zhang, T.T., Yan, E.C., Hu, X.M., Cao, Y.B., 2012. Fractal Description of Rock Mass Structure Representative Elementary Volume. *Advanced Materials Research* **594-597**, 439-445.

Zuan Chen, Z., Jin, Z.H. & Johnson, S.E. (2011). Transient dyke propagation and arrest near the level of neutral buoyancy. *Journal of Volcanology and Geothermal Research* **203**, 81-86.

Tables

Table 1. 2D textural results.

sample label	distance from wall-rock (cm)	phase	> 1 mm (area %)	> 0.1 and ≤ 1 mm (area%)	< 0.1/0.2 mm (area%)	2D whole amount (area%)	#/mm^{-2}
		facility	HRS	TOM	BS-SEM		
DK1	0	bubbles	0.4	10.8 (3.2)	-	11.2	3.50
		plg	-	-	63.9 (1.7)	63.9	-
		cpx	-	-	19.8 (1.4)	19.8	4113
		ol	-	-	1.6 (0.8)	1.6	1076
		timt	-	-	3.5 (0.9)	3.5	1192
DK2	36	bubbles	10.5	9.1 (3.4)	-	19.6	0.69
		plg	-	-	57.9 (2.3)	57.9	-
		cpx	-	-	16.6 (2.8)	16.6	2491
		ol	-	-	2.0 (0.4)	2.0	1097
		timt	-	-	3.9 (0.8)	3.9	727
DK3	72	bubbles	5.4	3.6 (4.5)	-	8.9	0.31
		plg	-	-	64.8 (2.4)	64.8	-
		cpx	-	-	16.3 (1.6)	16.3	2651
		ol	-	-	3.0 (0.7)	3.0	1812
		timt	-	-	7.0 (1.6)	7.0	1401
DK4	108	bubbles	13.6	12.8 (3.5)	-	26.4	0.90
		plg	-	-	52.3 (2.4)	52.3	-
		cpx	-	-	14.0 (1.1)	14.0	1853
		ol	-	-	3.8 (1.0)	3.8	1280
		timt	-	-	3.5 (0.8)	3.5	441
DK5	144	bubbles	27.4	1.6 (2.1)	-	29.0	0.21
		plg	-	-	47.9 (2.5)	47.9	-
		cpx	-	-	13.4 (1.8)	13.4	1443
		ol	-	-	4.8 (2.2)	4.8	1291
		timt	-	-	4.9 (1.4)	4.9	680
DK6	180	bubbles	8.5	0.7 (0.8)	-	9.2	0.15
		plg	-	-	61.0 (0.8)	61.0	-
		cpx	-	-	18.7 (2.4)	18.7	1349
		ol	-	-	6.2 (0.9)	6.2	1609
		timt	-	-	4.9 (0.9)	4.9	426
DK7	216	bubbles	20.9	1.3 (1.4)	-	22.2	0.23
		plg	-	-	54.9 (3.6)	54.9	-
		cpx	-	-	15.3 (2.6)	15.3	1423
		ol	-	-	4.5 (0.5)	4.5	1614
		timt	-	-	3.0 (0.6)	3.0	423

Footnotes. Crystals were measured only by BS-SEM, whereas bubbles only by HRS and TOM due to their sizes > 0.1 mm.

Table 2. 3D analytical conditions.

sample label	d_1 (mm)	d_2 (mm)	volume (cm^3)	tube Voltage (kV)	current (µA)	filter	voxel size (µm)	number of projections	angle of rotation (deg)	exposure time (s)
DK1	100	400	10.8	130	61	1.5 mm Al	6.25	2400	360	6.5
DK2	80	250	5.3	130	61	1.5 mm Al	8	1800	360	4
DK3	80	250	3.8	130	61	1.5 mm Al	8	1800	360	4
DK4	80	250	10.1	130	61	1.5 mm Al	8	1800	360	4
DK5	100	400	4.2	130	61	1.5 mm Al	6.25	2400	360	6.5
DK6	80	250	6.2	130	61	1.5 mm Al	8	1800	360	4
DK7	80	250	6.3	130	61	1.5 mm Al	8	1800	360	4

Footnotes. Experimental parameters used for the X-ray µCT scans. d_1 = source to sample distance; d_2 = source to detector distance.

Table 3. 3D textural results.

sample label		DK1	DK2	DK3	DK4	DK5	DK6	DK7
voxels		651× 516× 857×	796× 1122× 1270×	826× 990× 1280×	667× 1374× 1280×	468× 1080× 1270×	598× 916× 1270×	740× 924× 1270×
isotropic-voxel length (mm)		0.0063	0.0080	0.0080	0.0080	0.0063	0.0080	0.0080
volume (mm^3)		70.3	580.7	535.9	600.6	156.7	356.2	444.6
volume %	bubbles	10.9	16.8	12.2	13.9	22.9	10.8	19.4
	timt	2.2	2.3	2.3	2.5	2.0	2.3	2.1
number (#)	bubbles	4143	729	2993	781	2495	353	389
	timt	6338	30470	33356	47302	17505	24965	35120
number per volume ($\#/mm^{-3}$)	bubbles	58.9	1.3	5.6	1.3	15.9	1.0	0.9
	timt	90.2	52.5	62.2	78.8	111.7	70.1	79.0
average volume (mm^3)	bubbles	0.002	0.133	0.022	0.107	0.014	0.109	0.221
	timt	2×10^{-4}	4×10^{-4}	4×10^{-4}	3×10^{-4}	2×10^{-4}	3×10^{-4}	3×10^{-4}
average aspect ratio	bubbles	0.25	0.38	0.33	0.35	0.22	0.36	0.36
average sphericity	bubbles	0.74	0.76	0.76	0.78	0.83	0.77	0.76
specific surface area (mm^{-1})	bubbles	4.5	0.6	0.6	0.3	0.1	0.2	0.3
integral of mean curvature (mm^{-2})	bubbles	53.1	2.3	4.5	1.1	2.5	0.9	1.0
Euler characteristic (mm^{-3})	bubbles	51.9	0.7	4.5	0.9	15.5	0.7	0.6
connectivity density	bubbles	-10.45	0.40	0.17	0.41	1.66	0.35	0.40
elongation index	bubbles	0.03	0.09	0.10	0.05	0.10	0.04	0.08
	timt	0.06	0.06	0.07	0.06	0.02	0.04	0.04
isotropy index	bubbles	0.73	0.74	0.70	0.71	0.78	0.71	0.77
	timt	0.93	0.88	0.89	0.90	0.90	0.90	0.89

Footnotes. Average aspect ratio: ratio between the longest and the shortest segment passing through the center of mass. Average sphericity: ratio of the diameter of the maximum inscribed sphere in a blob and the diameter of the sphere with the same volume as the blob. Specific surface area: ratio between surface of the objects and their volume. Integral of mean curvature: positive and negative value indicates the dominance of convex and concave objects (bubbles). Euler characteristic: index of connectivity of the object network (bubbles), where positive and negative values are indicative of isolated *vs* connected/aggregates objects (bubbles). Connectivity density: number of redundant connections normalized to the total volume, with negative and positive values indicative of low and high connection. Elongation index: it measures the preferred orientation of a fabric, varying between 0 (no preferred orientation) and 1 (perfect preferred). Isotropy index: similarity of fabric to a uniform distribution, changing between 0 (fully anisotropy) and 1 (perfect isotropy).

Figures

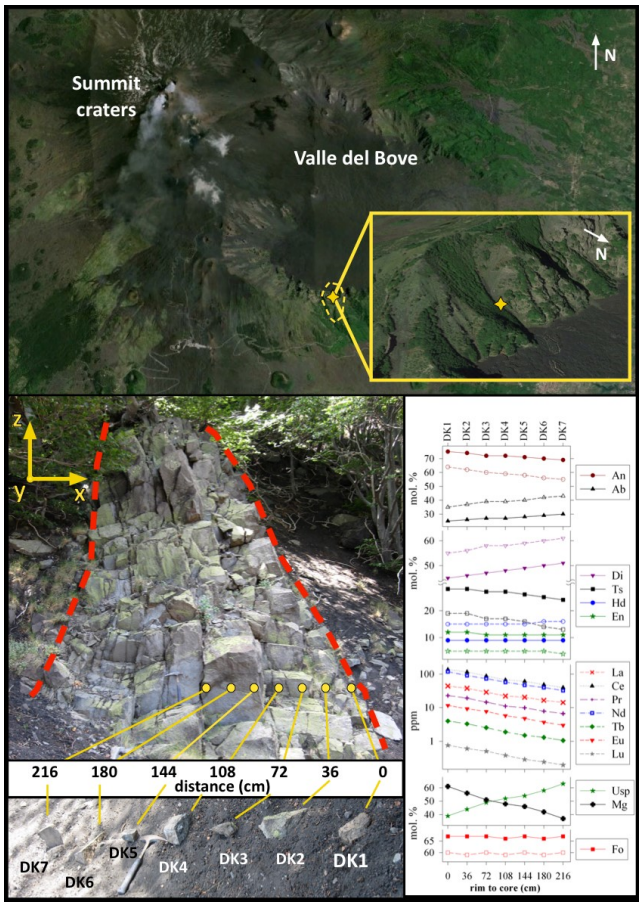

Fig. 1. a) Location of the dyke (yellow star) and the Canalone dei Faggi (yellow dashed line) plus its view (inset) (by Google Earth. b) The DK dyke in the field, with its contacts (red dashed lines) and the position of oriented collected DK samples. Z, X and Y are vertical, rim to rim (thickness) and normal to the plane dyke directions.

c) Stacked plots of molecular variations of cores and rims of minerals as a function of distance from the DK dyke right margin (from Mollo *et al.*, 2011); for cpx cores are also reported trace element variations (from Scarlato *et al.*, 2014). Symbols are An: anorthite. Ab: albite. Di: diopside. Ts: Tschermark. Hd: hedenbergite. En: enstatite. Us: ulvospinel. Mt: magnetite and Fo: fosterite. Trace elements reported are La: lanthanum. Ce: cerium. Pr: praseodymium. Nd: neodymium. Tb: terbium. Eu: europium. Lu: lutetium.

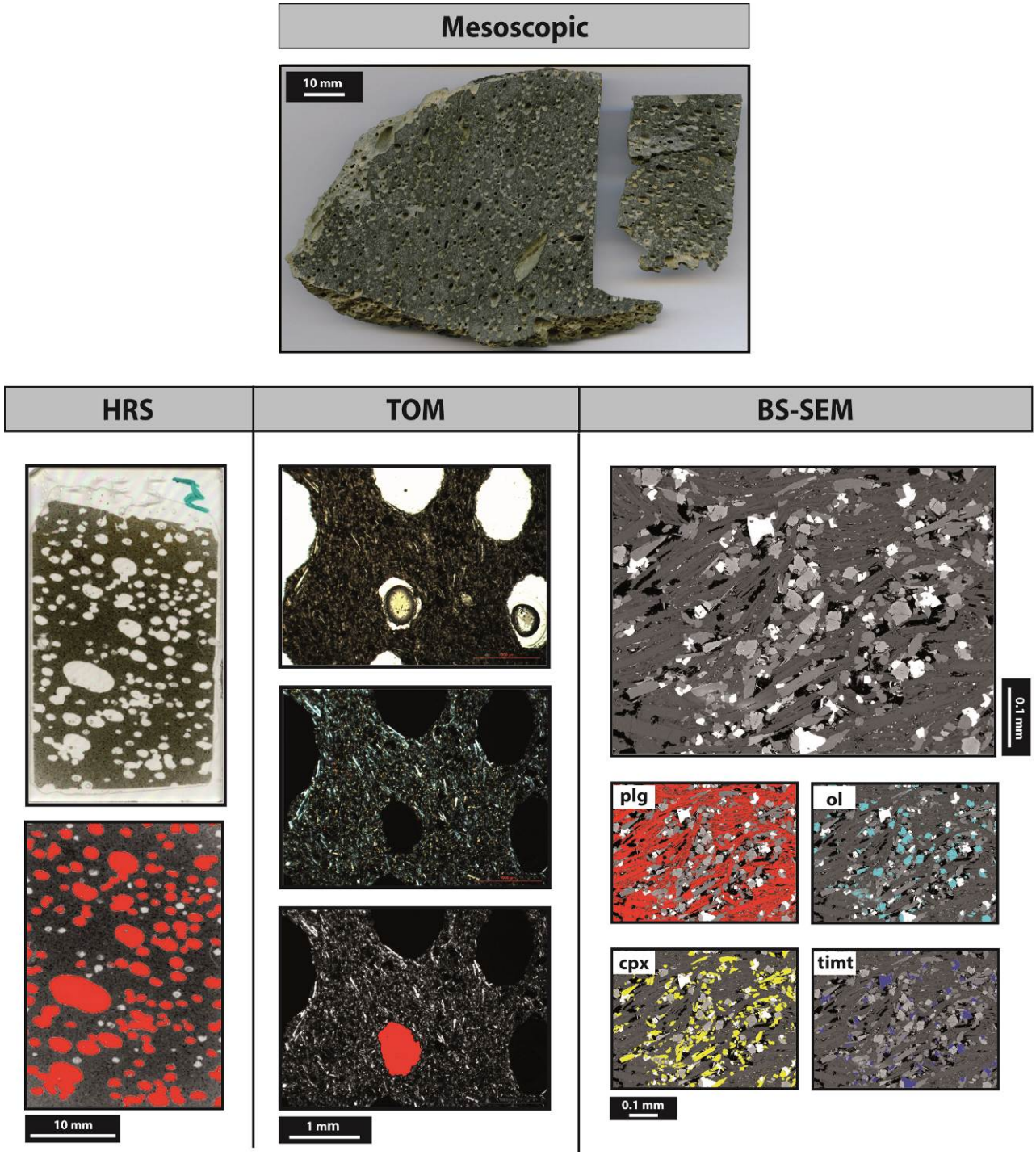

Fig. 2. Examples of 2D observations and segmentations of phases by image analysis. Top) Mesoscopic polished surface (DK5) used for general inspections of large phase and their dispositions in space. Down – left) HRS (high-resolution scanner) original scanned image (up) and its corresponding segmented (down) image used for counting phase > 1 mm (in red). Down – middle) TOM (transmission optical microscopy) parallel and cross polarizers digital images at 2.5× (up and middle) with segmented phases with sizes > 0.1 and ≤ 1 mm (in red). Down – right) BS-SEM (back-scattered scanning electron microscopy) original image at 200× (up) and the corresponding segmented phases smaller than 0.1/0.2 mm (down); false colours on HRS, TOM and BS-SEM are segmented bubbles in red, cpx in yellow, ol in cyan, timt in blue, and plg on only BS-SEM images in red. In this dyke bubbles lower than 0.1 mm are not observed or extremely rare, whereas single crystal never exceeds length of 0.1 and 0.2 mm.

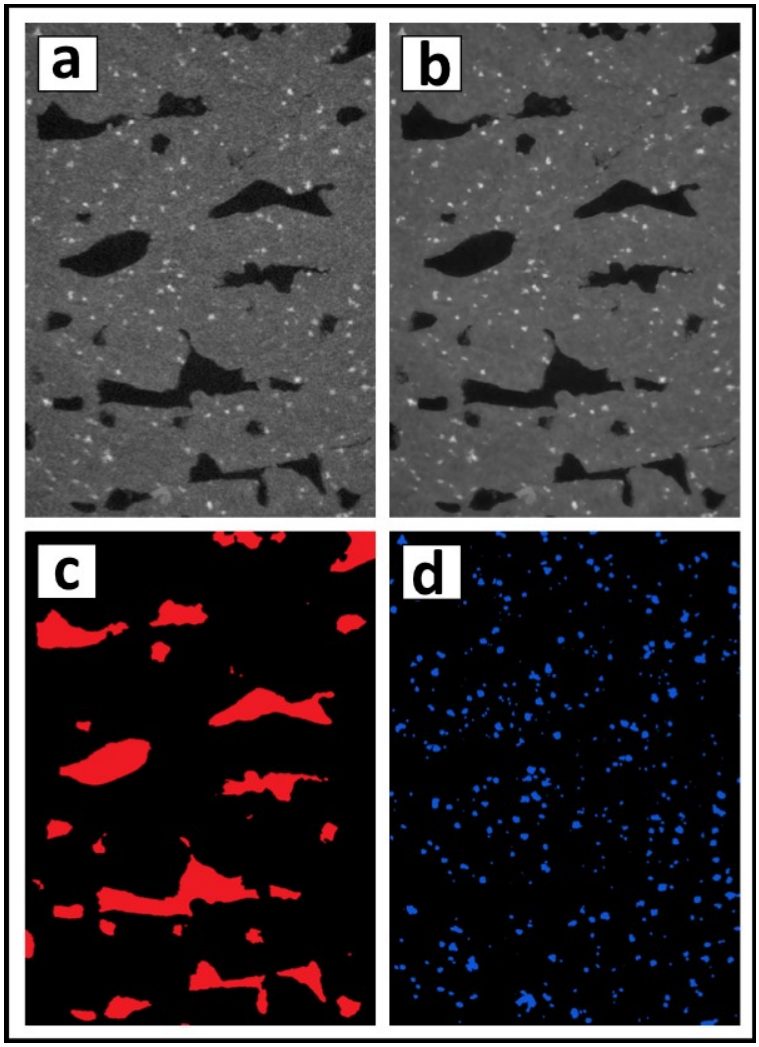

Fig. 3. Example of the *Pore3D* image analysis protocol applied to sample DK2. : a) portion of a reconstructed axial slice; b) filtered image with an “anisotropic diffusion filter”; c) threshold bubbles (c) and timt (d) by a 3D MultiOtsu filtering.

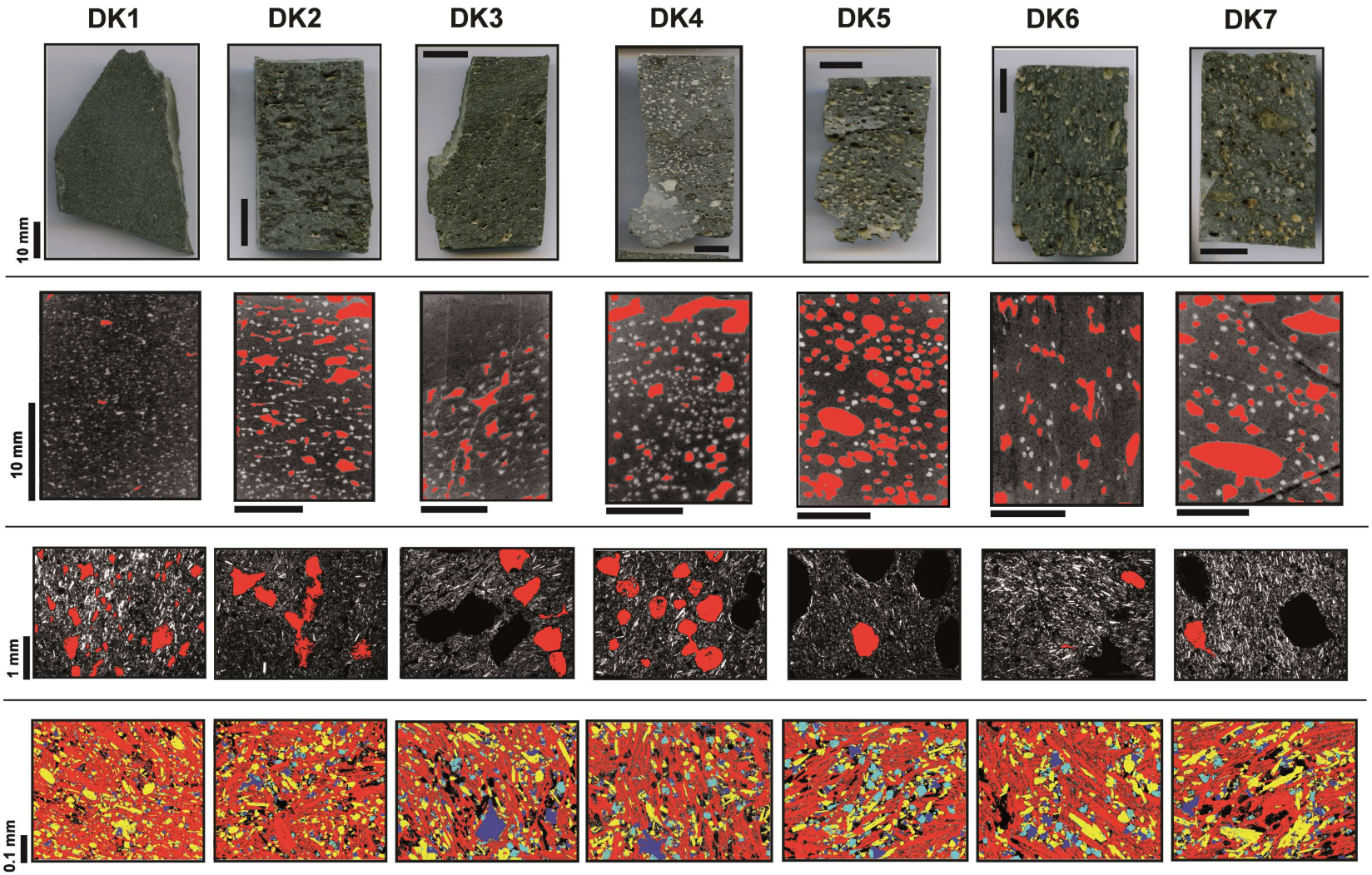

Fig. 4. Original and segmented textural features of DK samples at variable scales. First, second, third and fourth rows from top to down show: i) mesoscopic attributes on polished rock surfaces (some 10^3 mm^2), ii) HRS images of the polished thin sections (~ 10^2 mm^2), iii) TOM segmented images at 2.5 X (~ 10^1 mm^2) and iv) BSE-SEM segmented pictures (~10^{-1} to 10^{-2} mm^2). Bubbles have dimensions > 0.1 mm (red colors in second and third rows), whereas crystals (fourth row) have sizes ≤ 0.1/0.2 mm (plg: red. cpx: yellow. ol: cyan and timt: blue). The short and long edges of thin sections (second row) are coaxial with Z and X directions (see Fig. 1). More details are reported in the supplementary Figs. 4S.

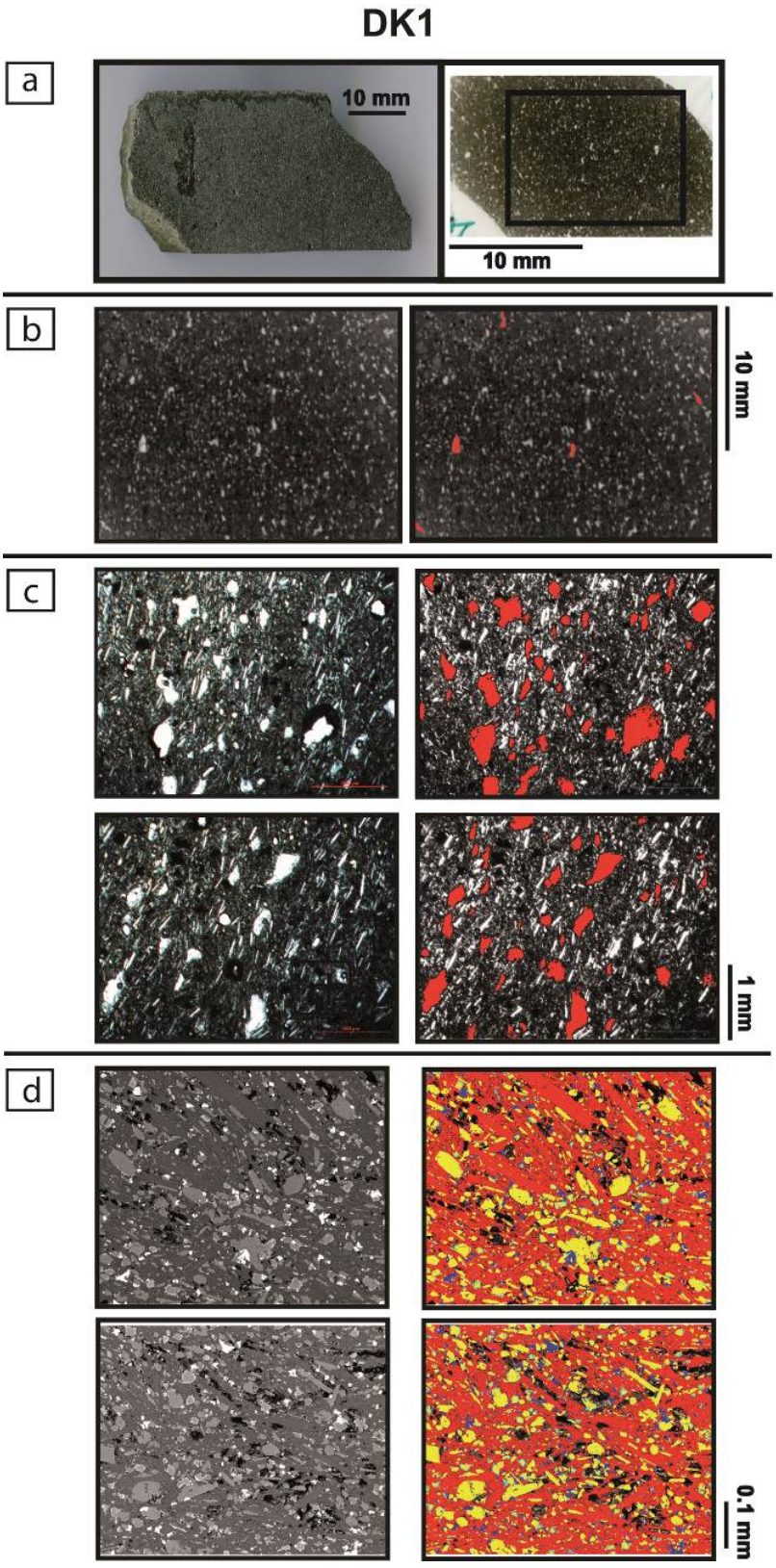

Fig. 4Sa. Textural details of the sample DK1. a) HRS polished mesoscopic surfaces and thin section. b) HRS original and segmented images of the thin section (red rectangle in a) for counting of phases > 1 mm; c) TOM original and segmented images at 2.5× for measurement of phases > 0.1 and ≤ 1 mm; d) BS-SEM original and segmented images at 130-270× for measurements of phases ≤ 0.1-0.2 mm, tiny voids are scratched crystals during grinding whereas false colours refer to plg: red, cpx: yellow, ol: cyan and timt: blue.

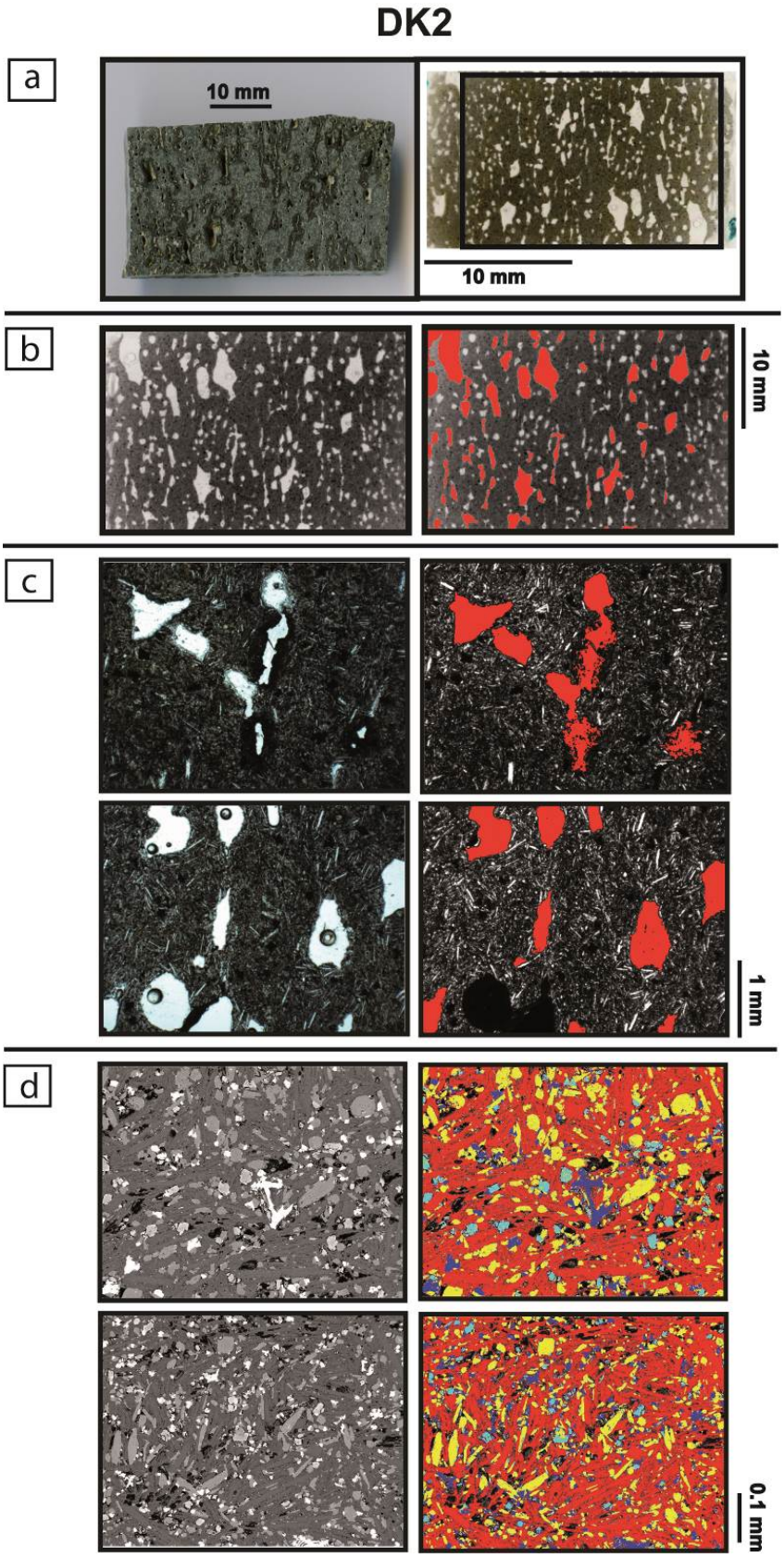

Fig. 4Sb. Textural details of the sample DK2. a) HRS polished mesoscopic surfaces and thin section. b) HRS original and segmented images of the thin section (red rectangle in a) for counting of phases > 1 mm; c) TOM original and segmented images at 2.5× for measurement of phases > 0.1 and ≤ 1 mm; d) BS-SEM original and segmented images at 130-270× for measurements of phases ≤ 0.1/0.2 mm, tiny voids are scratched crystals during grinding whereas false colors refer to plg: red, cpx: yellow, ol: cyan and timt: blue.

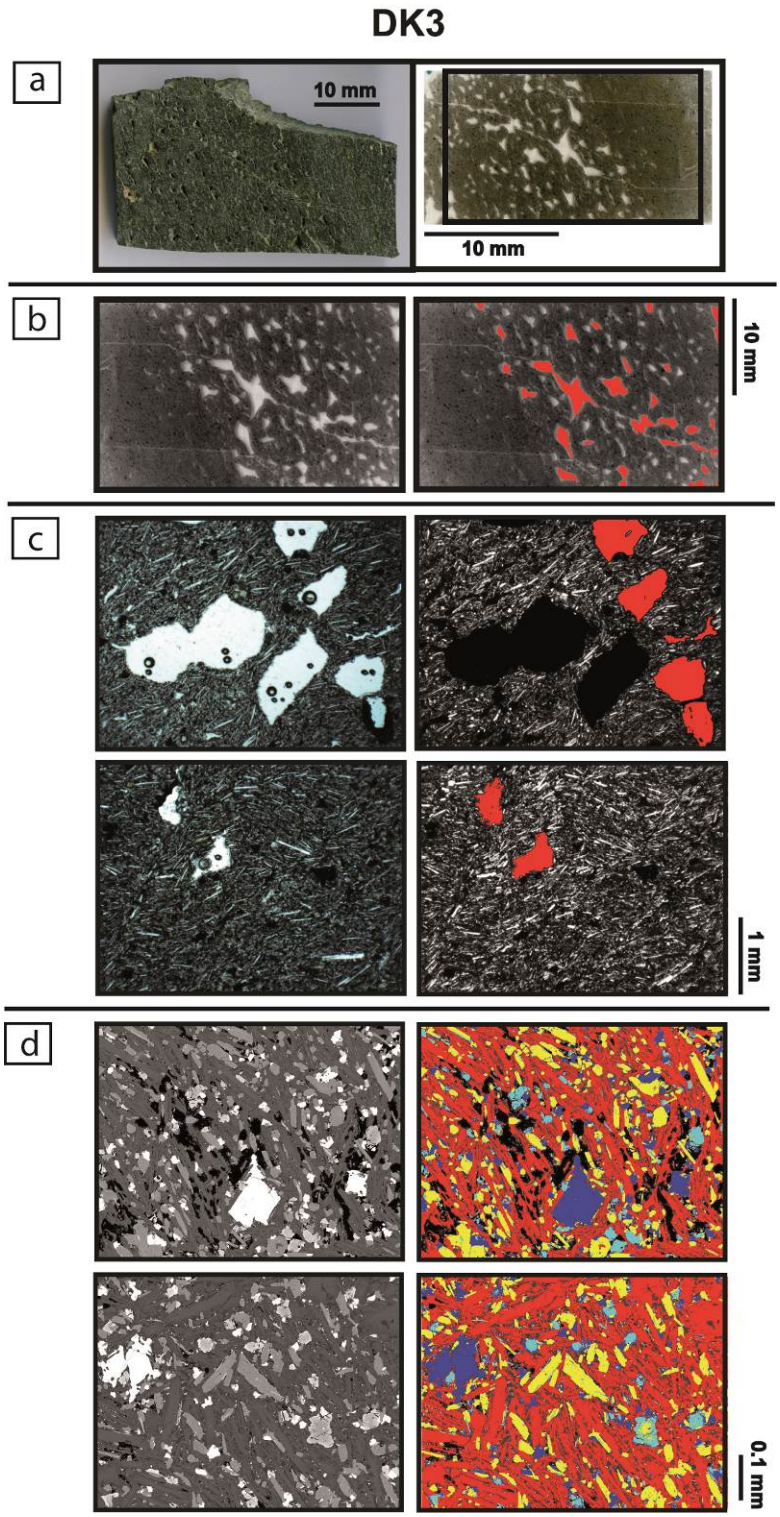

Fig. 4Sc. Textural details of the sample DK3. a) HRS polished mesoscopic surfaces and thin section. b) HRS original and segmented images of the thin section (red rectangle in a) for counting of phases > 1 mm; c) TOM original and segmented images at 2.5× for measurement of phases > 0.1 and ≤ 1 mm; d) BS-SEM original and segmented images at 130-270× for measurements of phases ≤ 0.1/0.2 mm, tiny voids are scratched crystals during grinding whereas false colors refer to plg: red, cpx: yellow, ol: cyan and timt: blue.

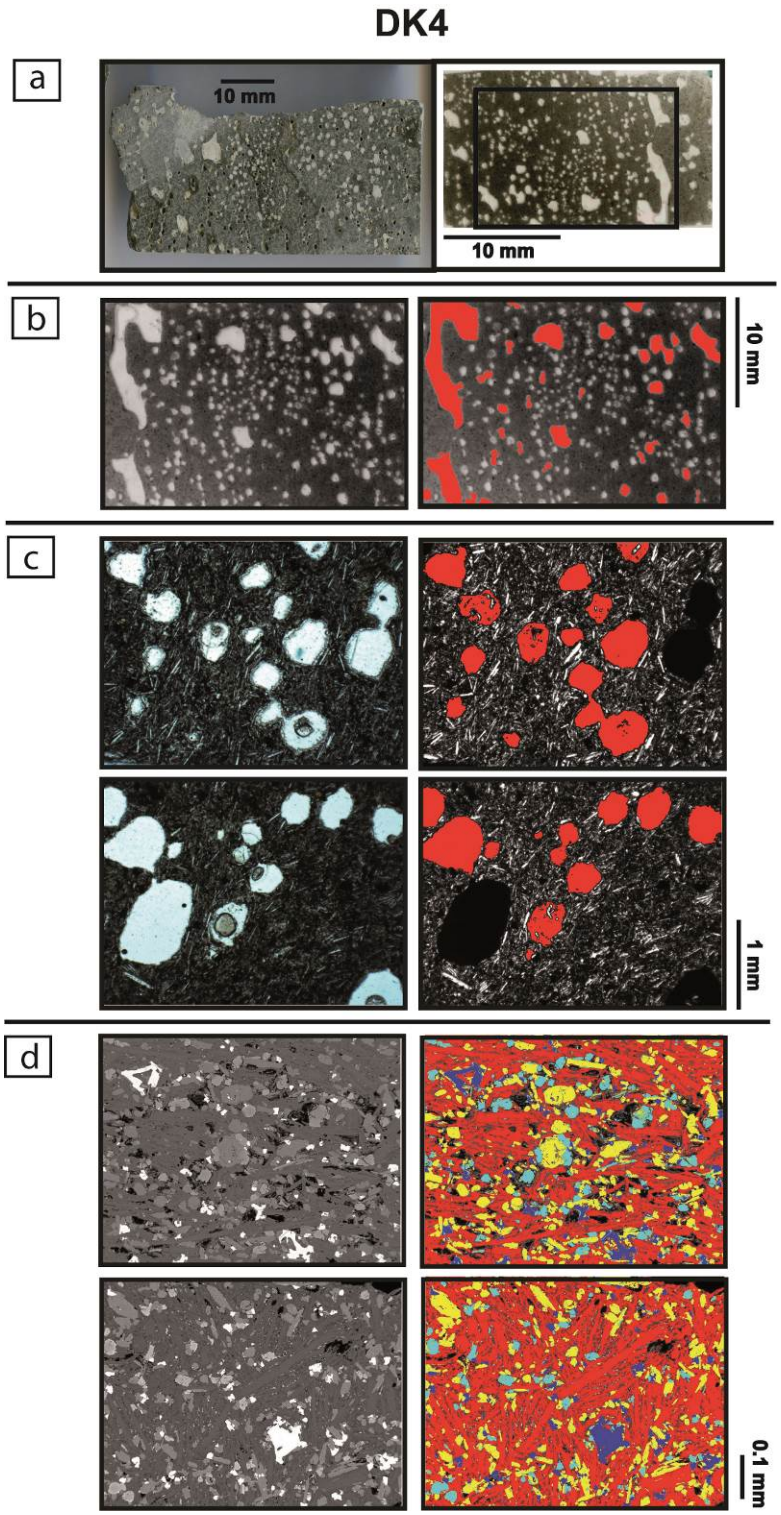

Fig. 4Sd. Textural details of the sample DK4. a) HRS polished mesoscopic surfaces and thin section. b) HRS original and segmented images of the thin section (red rectangle in a) for counting of phases > 1 mm; c) TOM original and segmented images at 2.5× for measurement of phases > 0.1 and ≤ 1 mm; d) BS-SEM original and segmented images at 130-270× for measurements of phases ≤ 0.1/0.2 mm, tiny voids are scratched crystals during grinding whereas false colors refer to plg: red, cpx: yellow, ol: cyan and timt: blue.

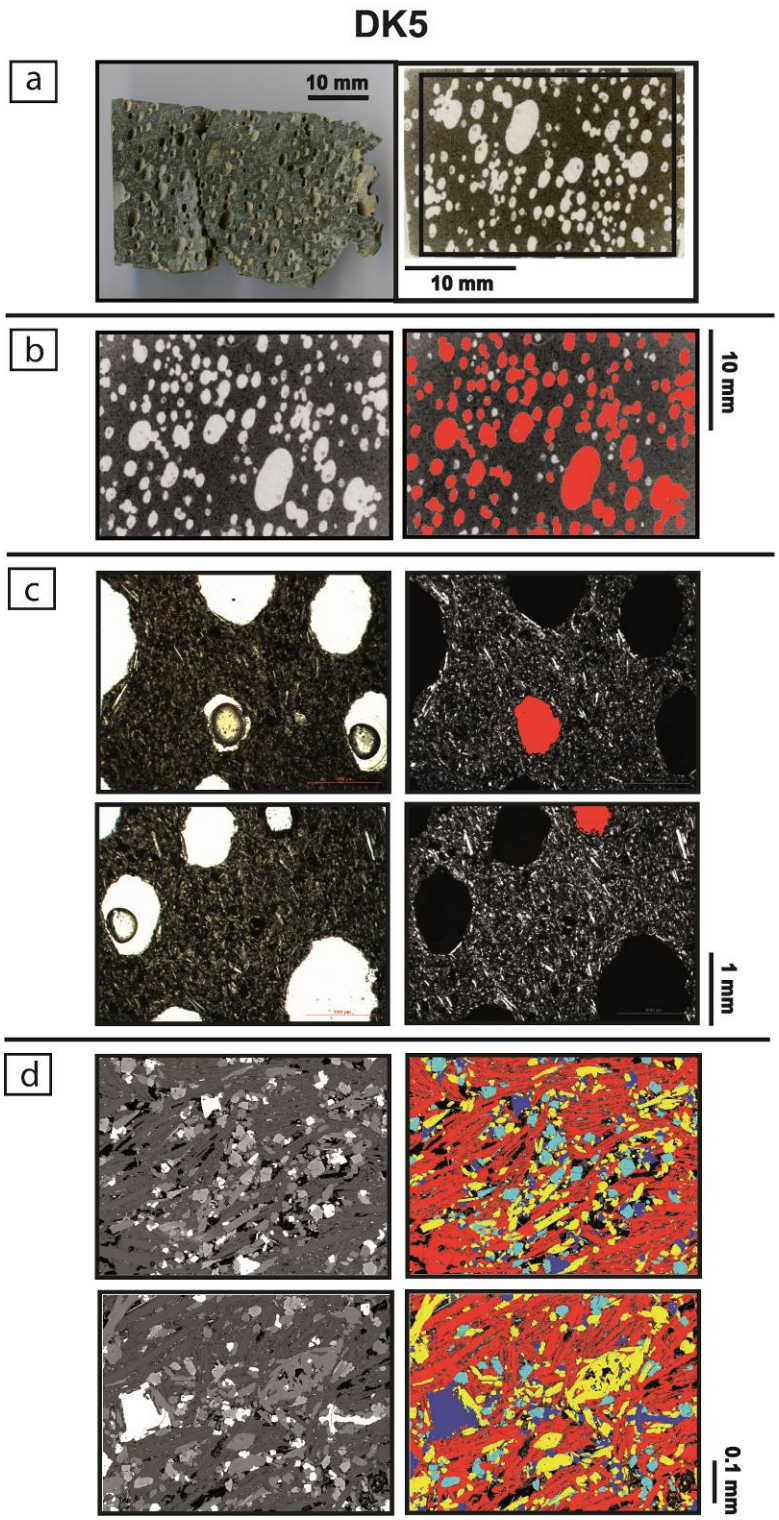

Fig. 4Se. Textural details of the sample DK5. a) HRS polished mesoscopic surfaces and thin section. b) HRS original and segmented images of the thin section (red rectangle in a) for counting of phases > 1 mm; c) TOM original and segmented images at 2.5× for measurement of phases > 0.1 and ≤ 1 mm; d) BS-SEM original and segmented images at 130-270× for measurements of phases ≤ 0.1/0.2 mm, tiny voids are scratched crystals during grinding whereas false colors refer to plg: red, cpx: yellow, ol: cyan and timt: blue.

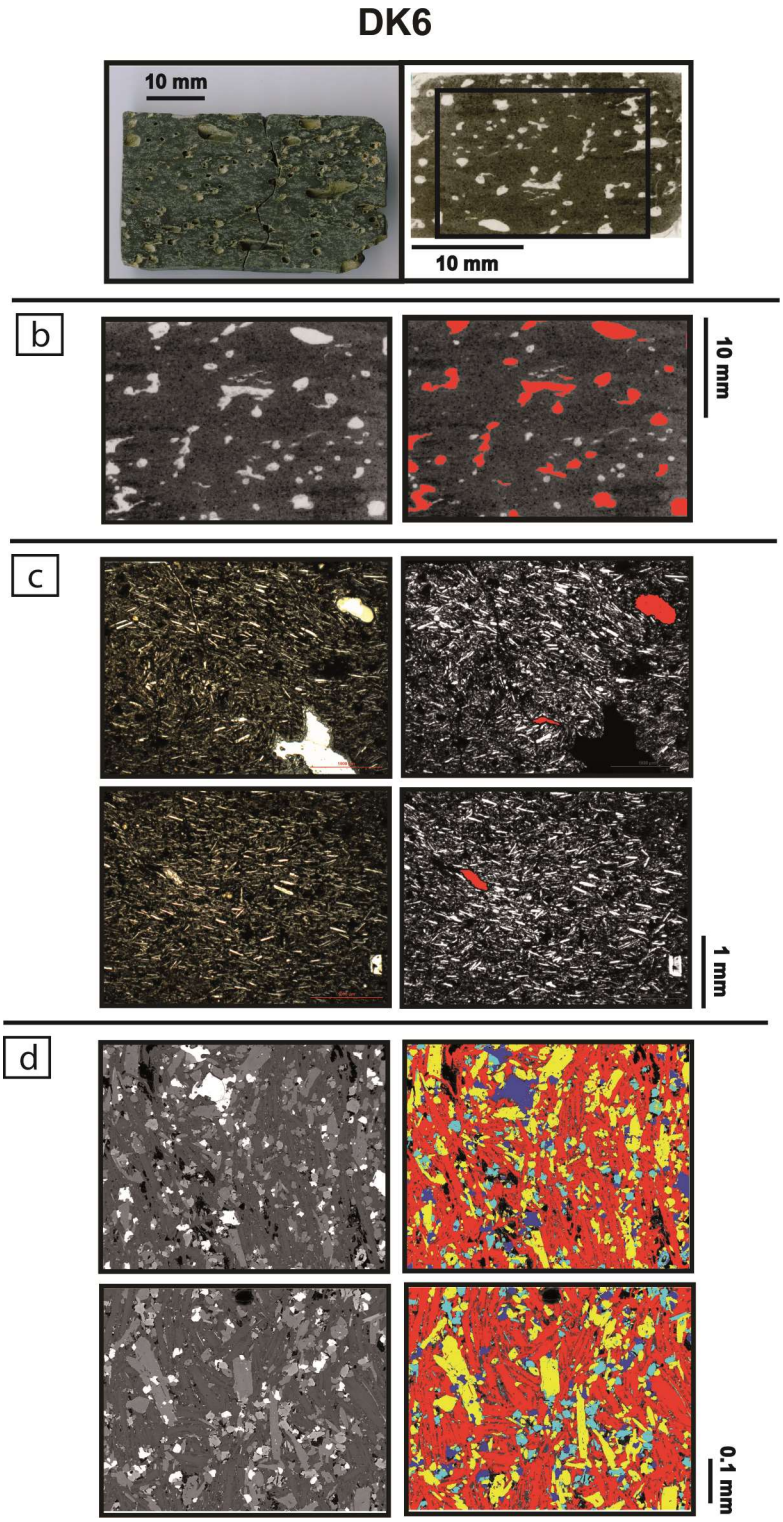

Fig. 4Sf. Textural details of the sample DK6. a) HRS polished mesoscopic surfaces and thin section. b) HRS original and segmented images of the thin section (red rectangle in a) for counting of phases > 1 mm; c) TOM original and segmented images at 2.5× for measurement of phases > 0.1 and ≤ 1 mm; d) BS-SEM original and segmented images at 130-270× for measurements of phases ≤ 0.1/0.2 mm, tiny voids are scratched crystals during grinding whereas false colors refer to plg: red, cpx: yellow, ol: cyan and timt: blue.

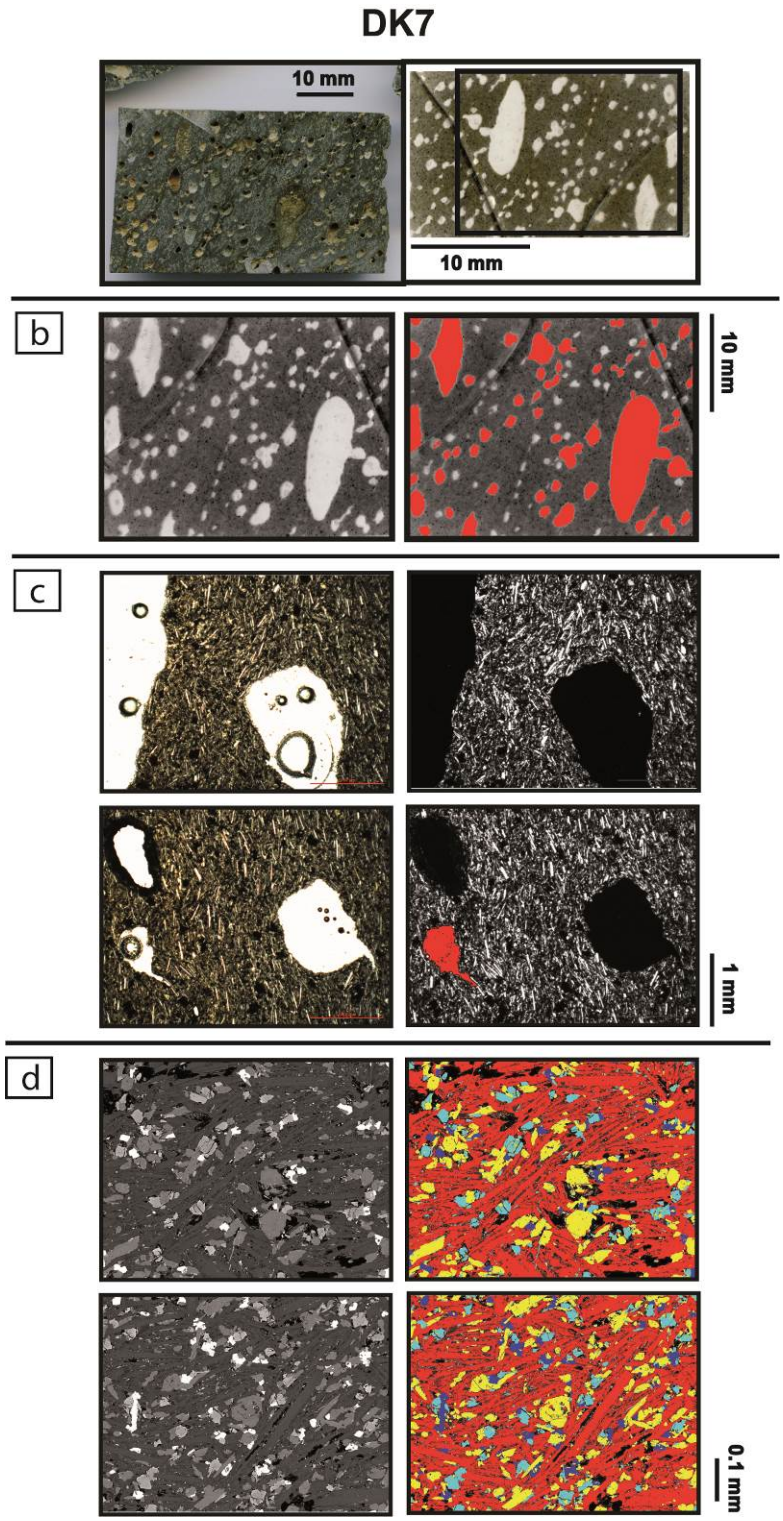

Fig. 4Sg. Textural details of the sample DK7. a) HRS polished mesoscopic surfaces and thin section. b) HRS original and segmented images of the thin section (red rectangle in a) for counting of phases > 1 mm; c) TOM original and segmented images at 2.5× for measurement of phases > 0.1 and ≤ 1 mm; d) BS-SEM original and segmented images at 130-270× for measurements of phases ≤ 0.1/0.2 mm, tiny voids are scratched crystals during grinding whereas false colors refer to plg: red, cpx: yellow, ol: cyan and timt: blue.

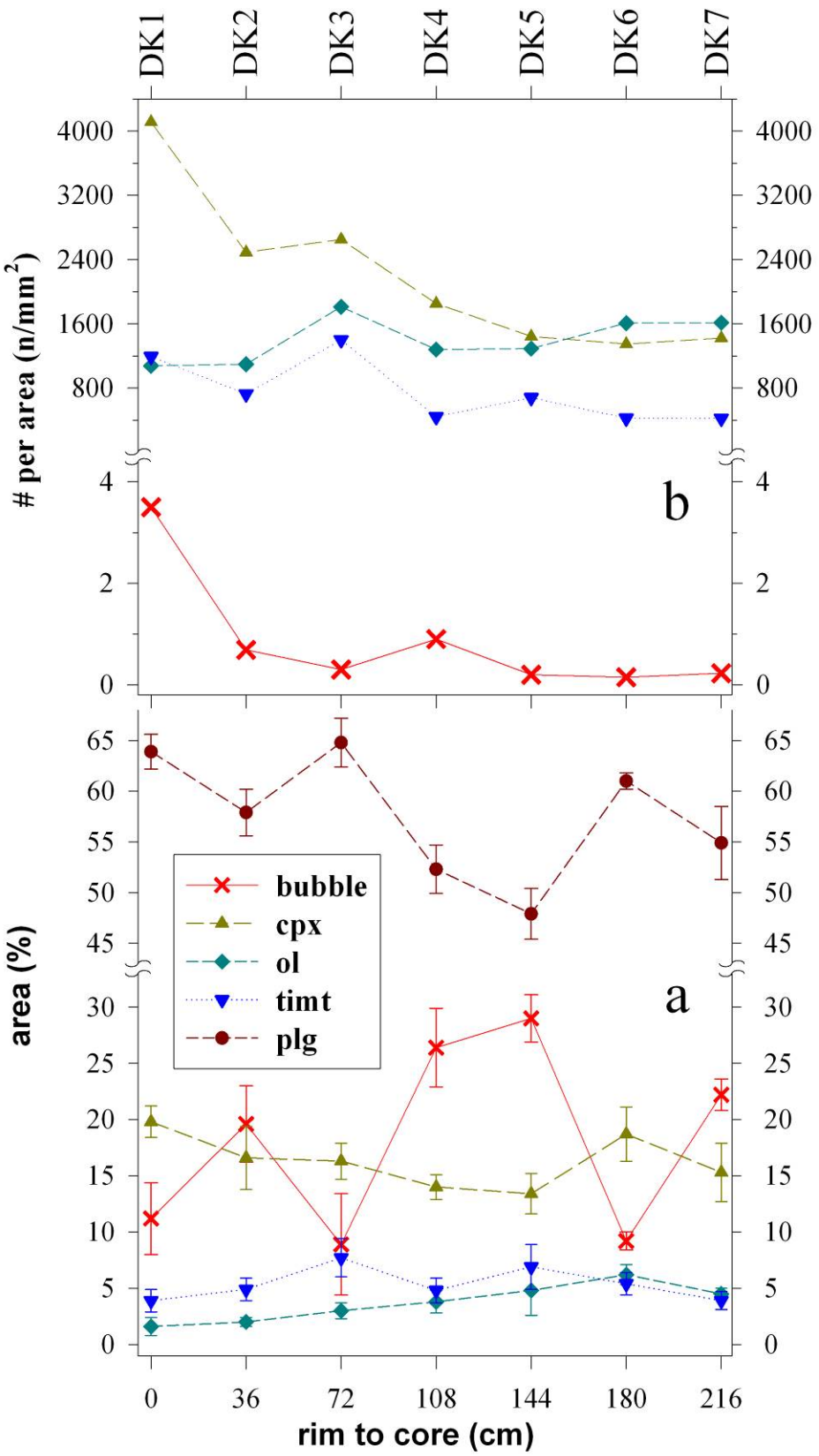

Fig. 5. Quantitative 2D textural features of DK rocks from rim to core. a) abundance of bubbles, plg, cpx, ol and timt; b) number of single bubble or mineral per unit area (#/mm^2).

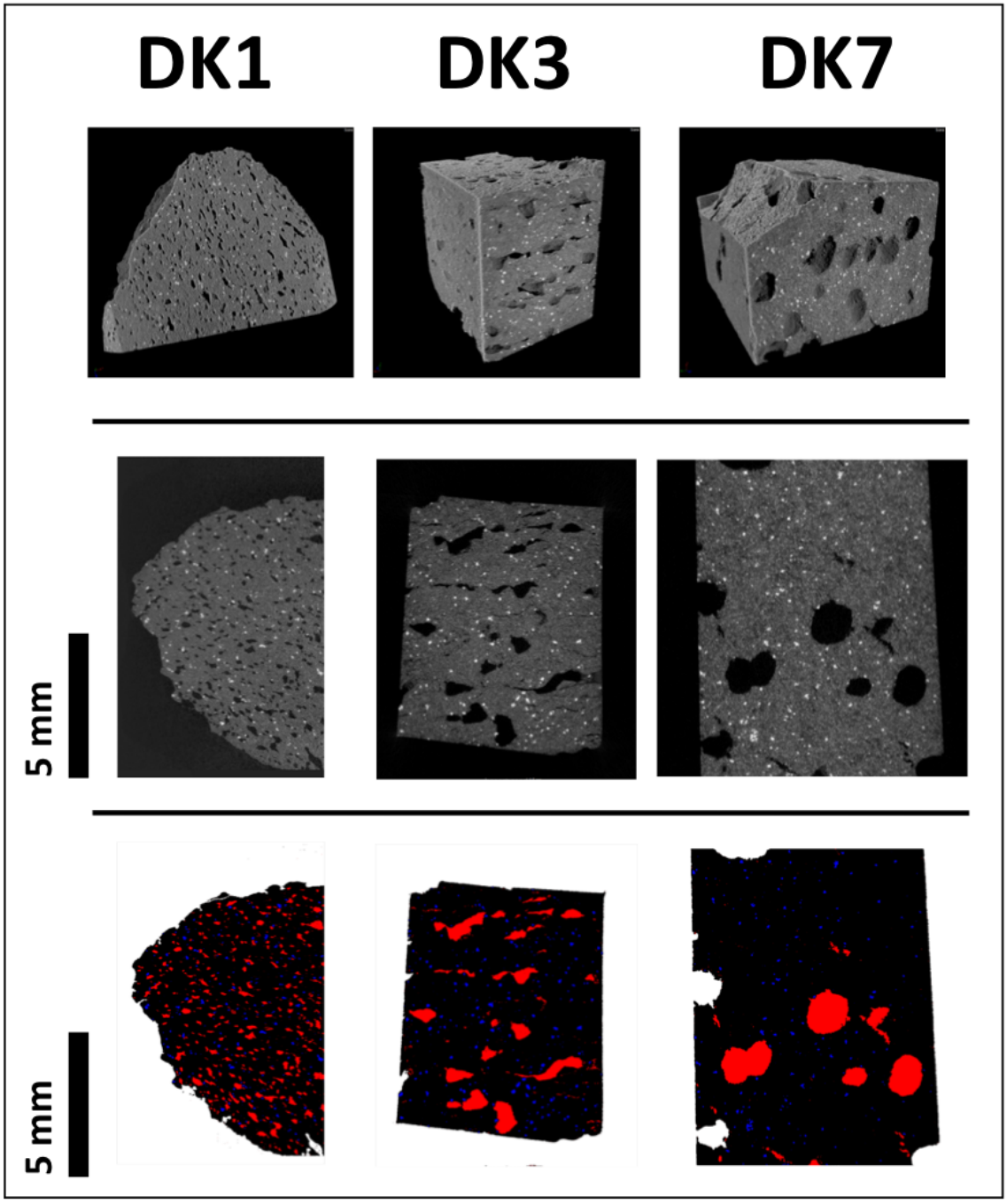

Fig. 6a. Up row: Volume renderings of the selected investigated samples. Middle row: reconstructed assail slices. Bottom row: the same slices reported in the middle row where bubbles (red) and timt (blue) not connected with the borders have been segmented.

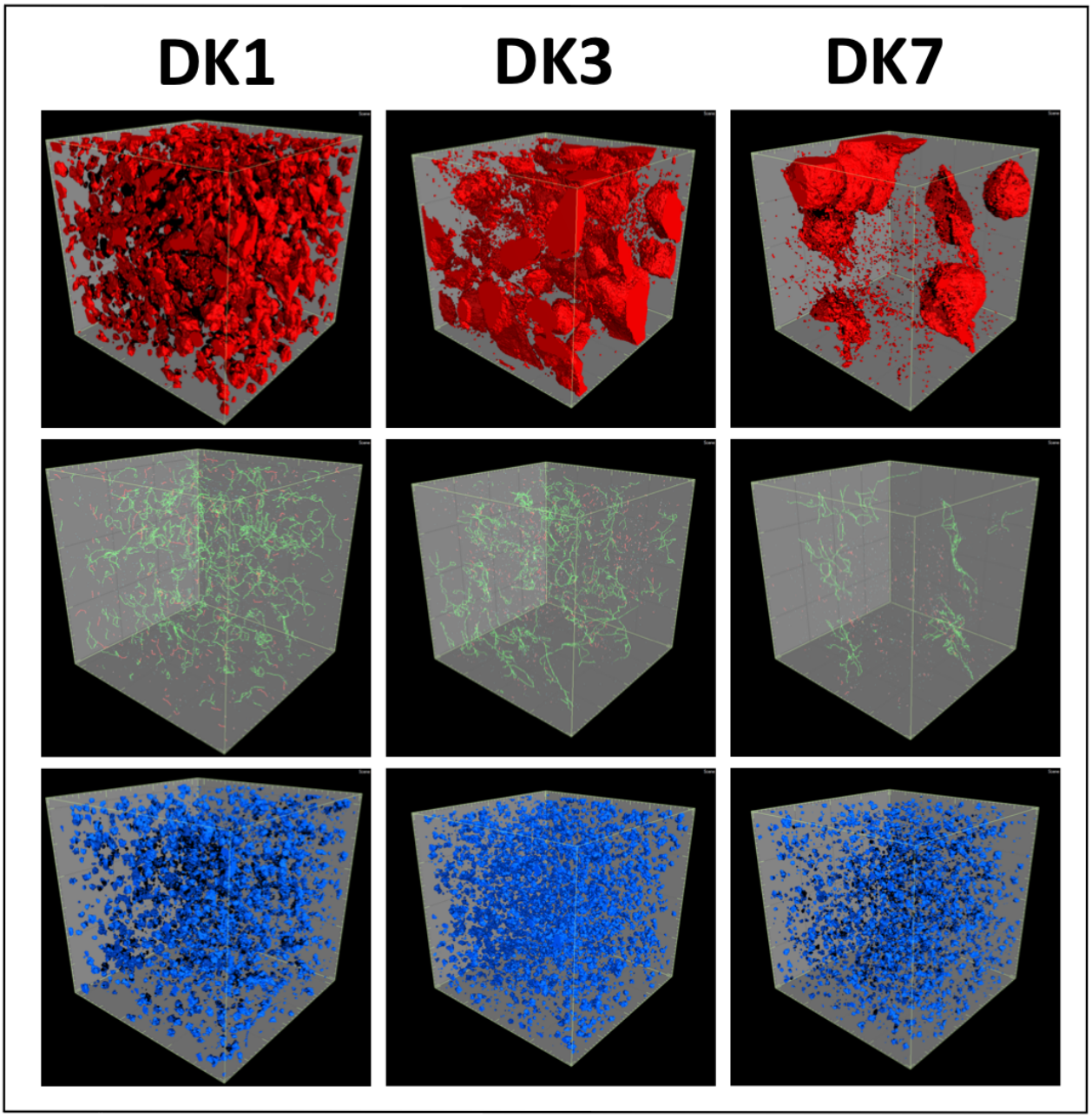

Fig. 6b. 3D renderings of 500×500×500 voxels volumes of selected samples. Up row: isosurface renderings of the bubble phase; Middle row: skeletons of the bubble network, in green node-to-node connections, in red end-to-end branches. Bottom row: isosurface rendering of the timt phase.

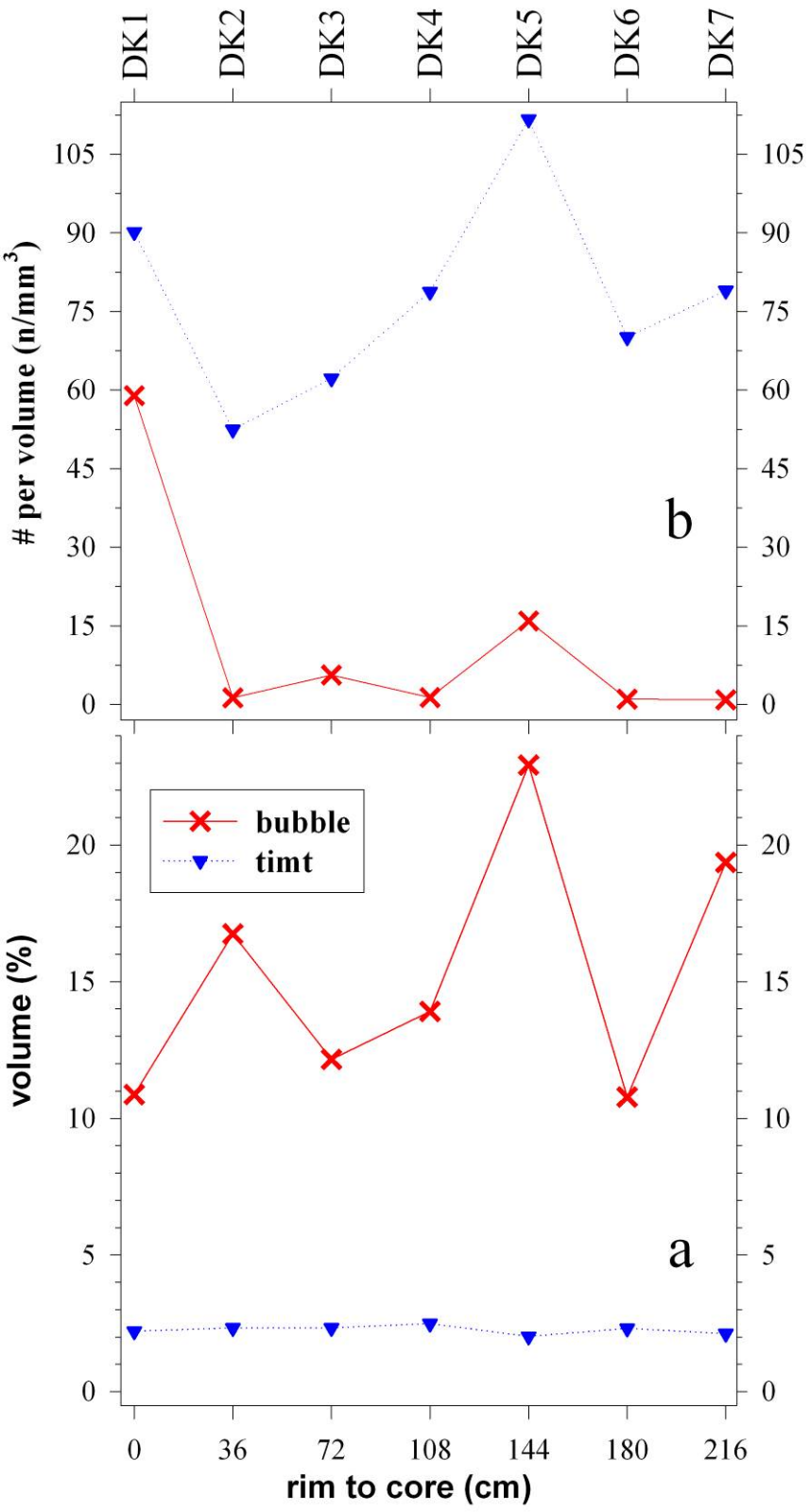

Fig. 7. Quantitative 3D textural features of dyke rocks from rim to core of it. a) Abundance of bubbles and timt. b) Number of single bubble and timt per unit volume (#/mm^3).

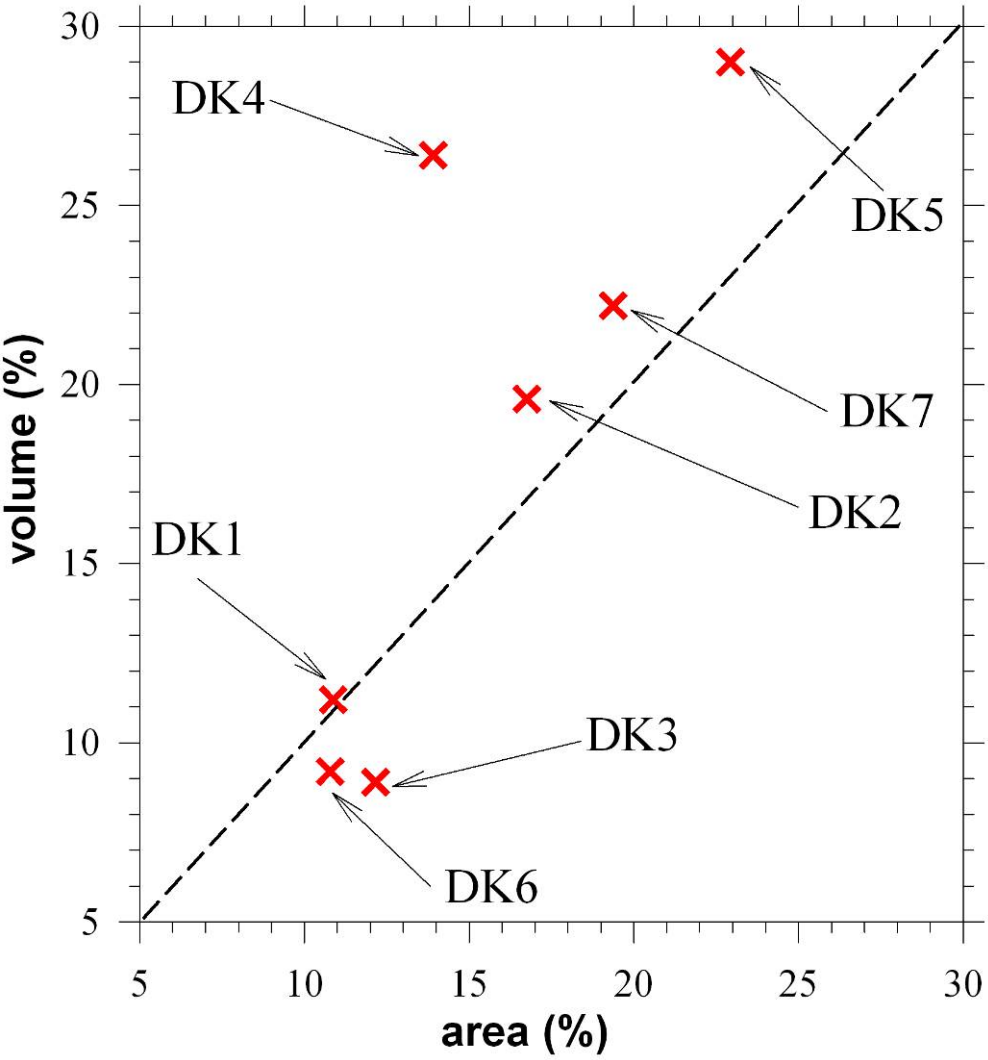

Fig. 8. Values of abundance of bubbles determined by 2D (area) and 3D (volume) image analyses. The dashed line is the 1:1 relation.

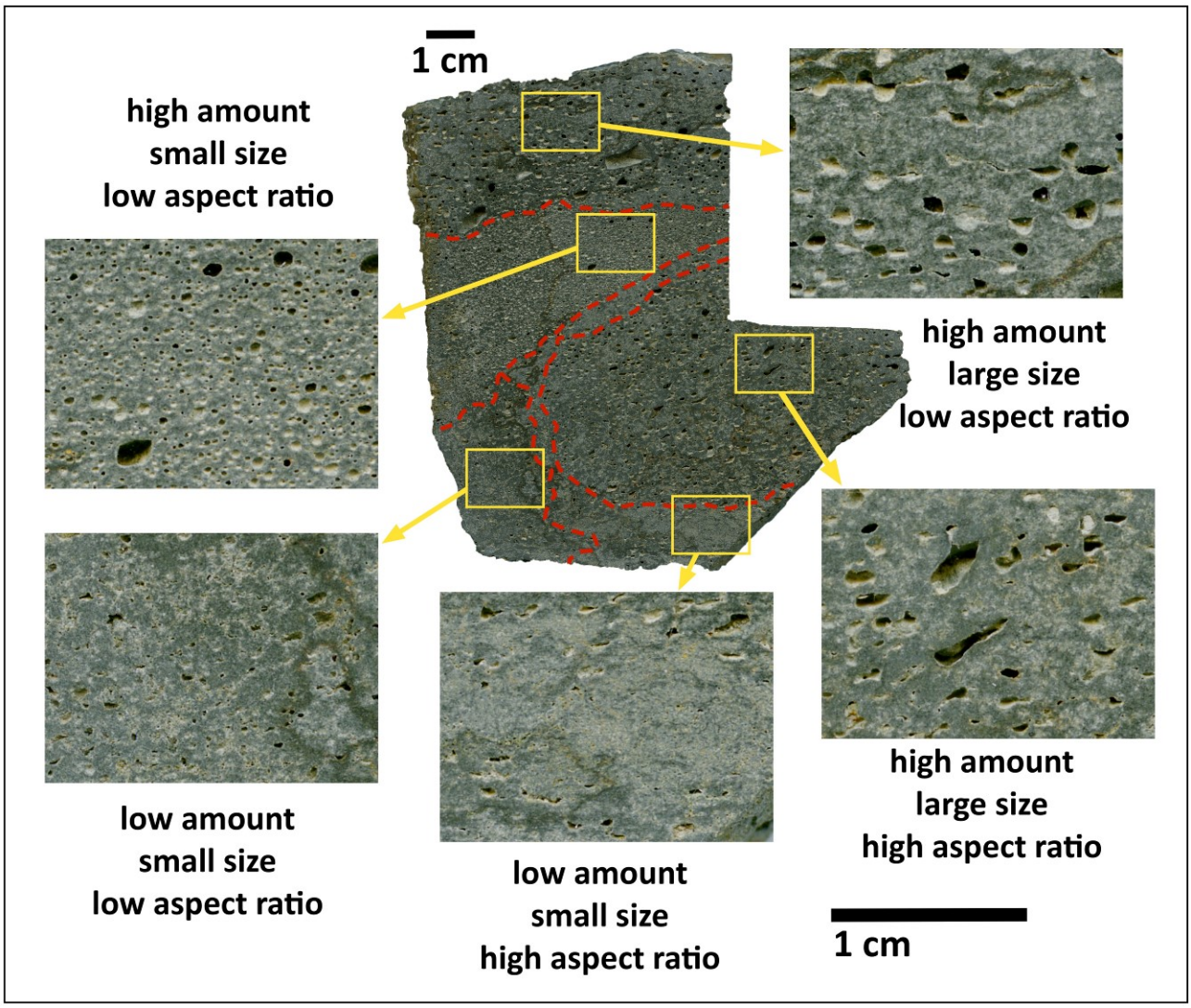

Fig. 9. DK4 large surface polished rock of about 8×10^3 mm^2. It shows coexistence of patches with marked variation in amount, size and aspect ratio (shape) of bubbles.

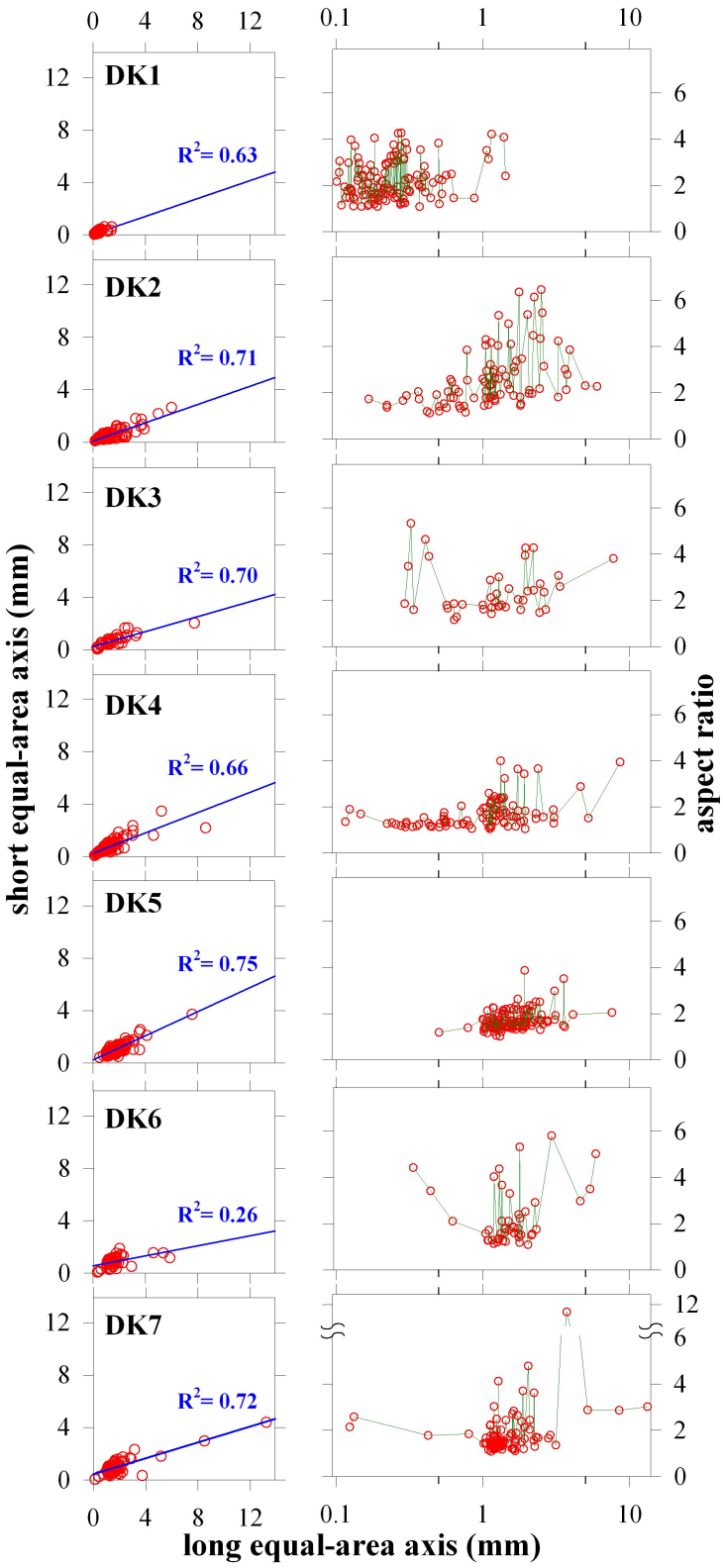

Fig. 10. Long *vs* short axes (left column) and long *vs* aspect ratios (right column) of equal-area ellipses of bubbles in 2D.

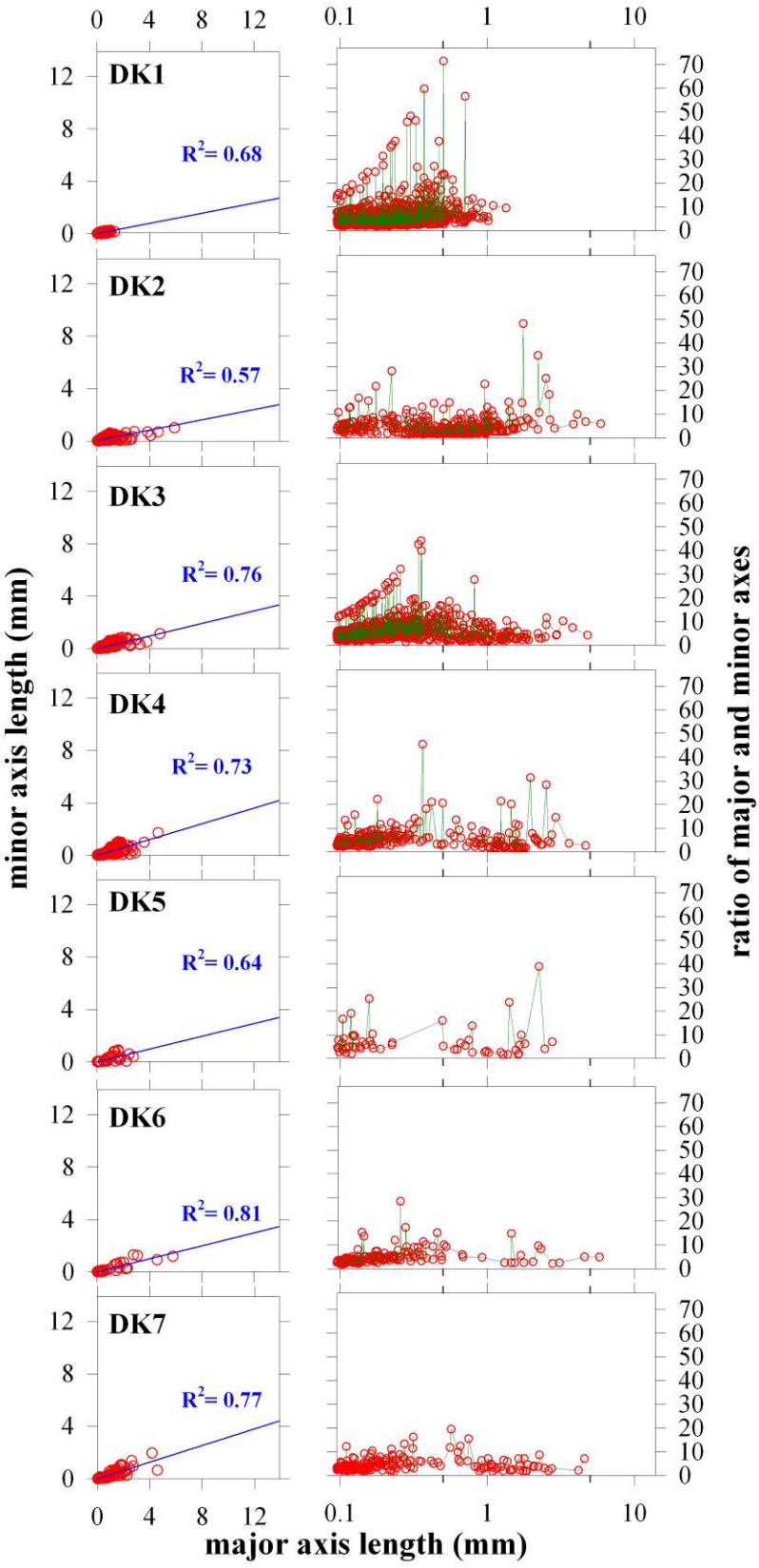

Fig. 11. Major *vs* minor axes length (left column) and major *vs* ratios of major/minor axes (right column) in 3D. The major and minor axes correspond to the longest and shortest segments included into each bubble and passing through its centre of mass.

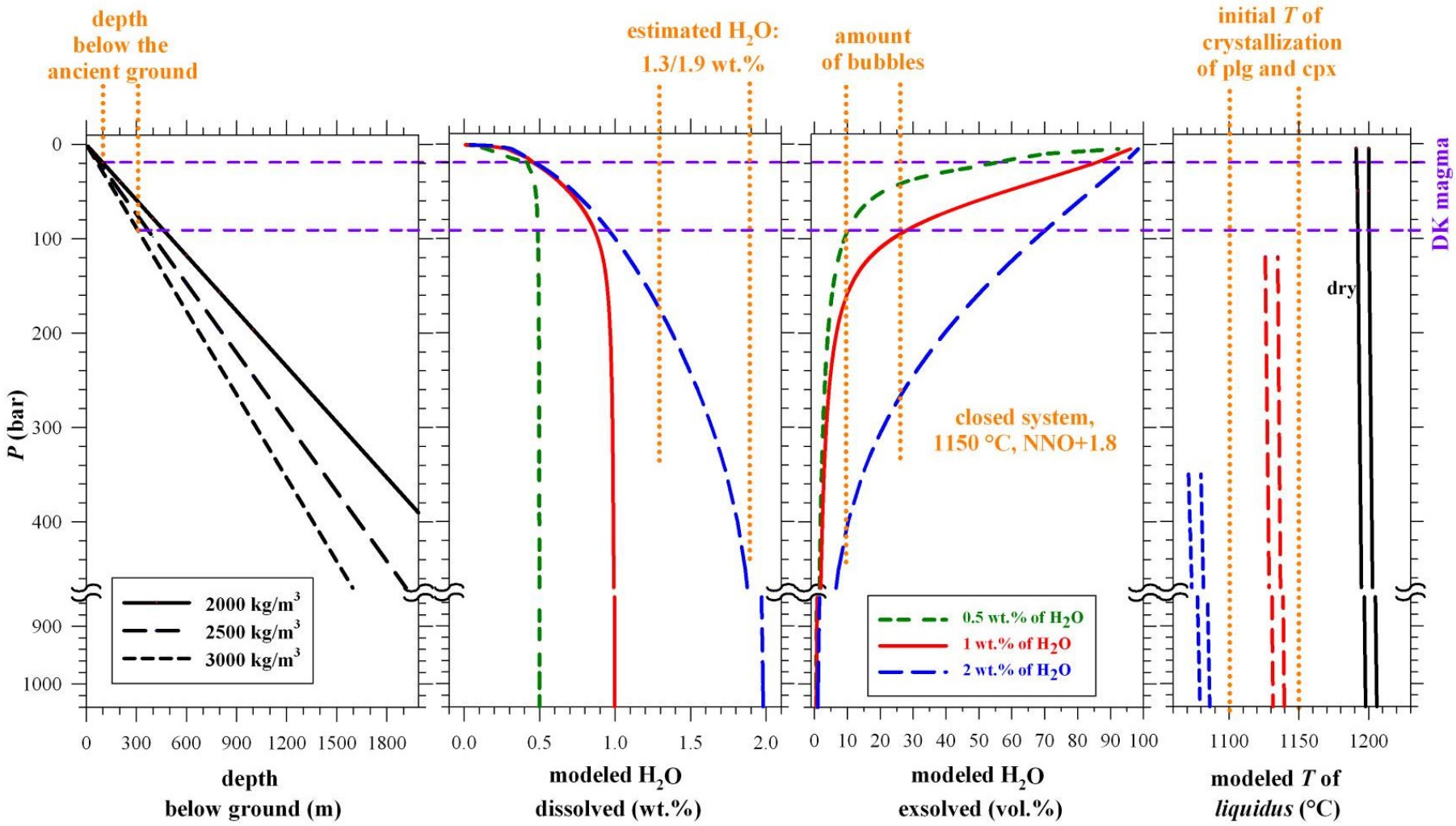

Fig. 12. Variation of physical parameters as a function of *P*. Left) Calculated *P* as a function of estimated 100/300 m overlying rocks with variable density (ρ_{rock}). Intermediate left) H_2O solubility modelled with SOLEX (Whitam *et al.*, 2012) for 0.5, 1 and 2 wt.% initial amount and the estimated amount by hygrometer (Mollo *et al.*,2011). Intermediate right) Modelled H_2O vol.% exsolution in a closed system, at *T* of 1150 °C and NNO+1.8 again using SOLEX for 0.5, 1 and 2 wt.% initial amounts and the range of bubble measured here (Tables. 1 and 3). Right) Estimated *liquidus* temperatures by Melts (Papale *et al.*, 2006) between NNO and QFM+3 for 1 and 2 wt.% of H_2O and anhydrous condition plus thermal ranges of onset of crystallization (Mollo *et al.*, 2011). The horizontal short-short violet lines indicate the pressure range for the DK magma at its ancient depth below the ground.

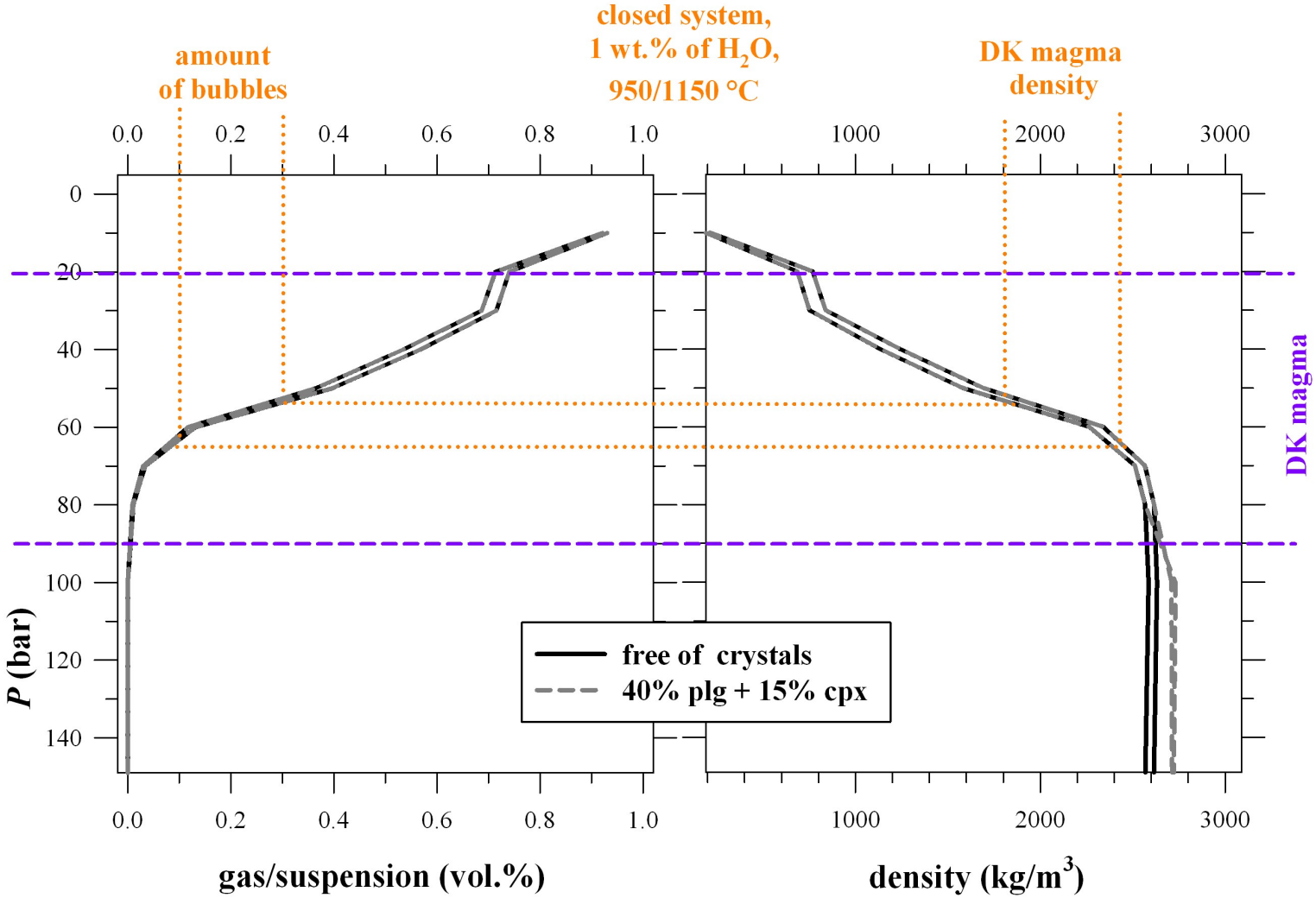

Fig. 13. Simulations of gas *vs* magmatic suspension ratio (left) and its density at relevant *P* (15 to 0 MPa), *T* (1150 to 950 °C), 1 wt.% of H_2O in a closed system and amount of crystals from 0 to 55 % (40% of plg + 15% of cpx). The simulations were performed using solubility model reported in Papale *et al.* (2006) that provides also gas/liquid partitions and moles of exsolved H_2O. These data were then used in the law of gases (see text and supplementary excel spreadsheets). The density of the DK magma is ≥ 2400 kg/m^3 below the DK magma and rapidly decreases to 1800 kg/m^3 to attain the measured range of bubbles. Density values lower than 1800 kg/m^3 are not possible for the DK magma.

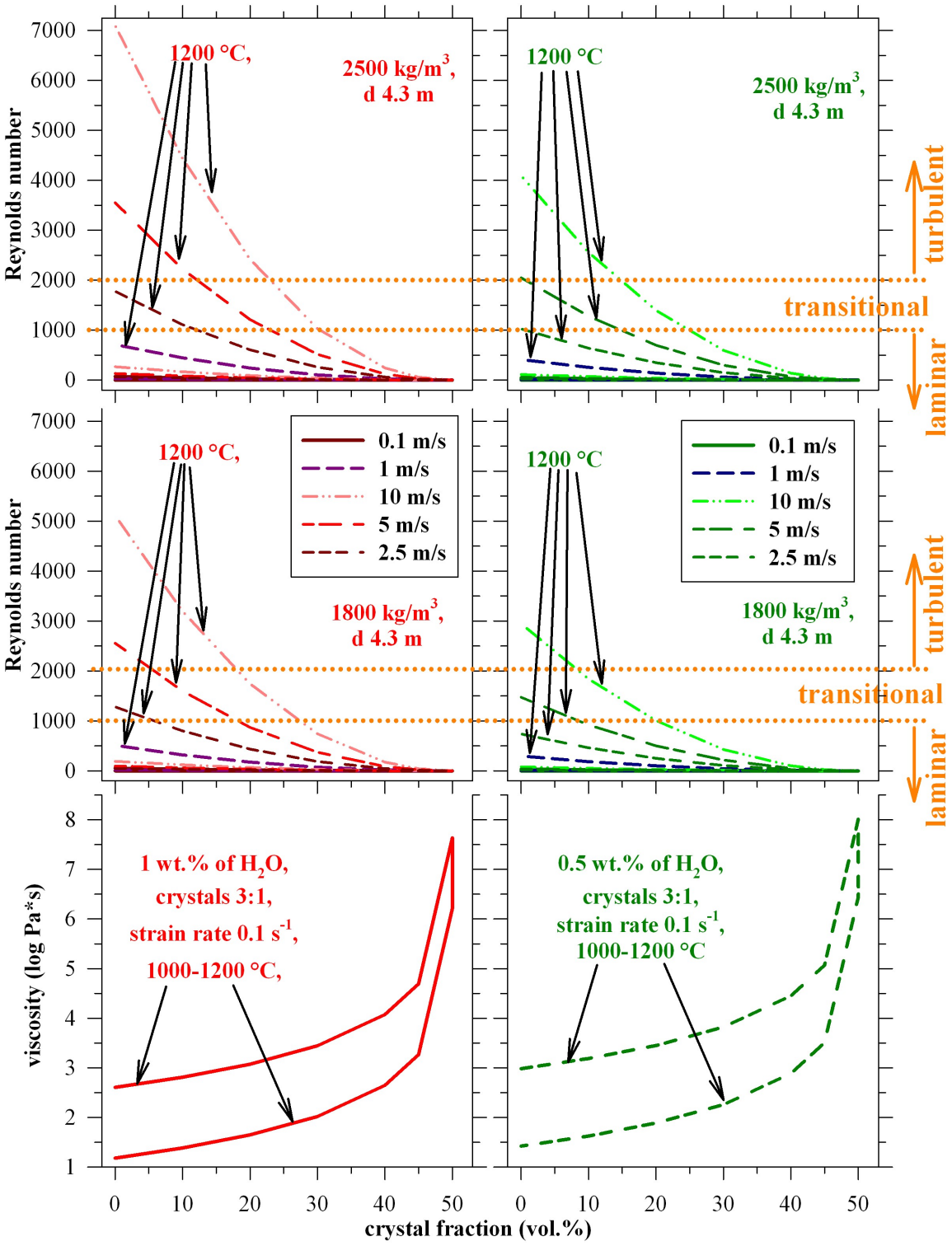

Fig. 14. (bottom) Simulations of viscosity for two magmatic suspensions with the liquid with a fixed compositions at the DK bulk one, between 1,200 and 1,000 °C, at a moderate strain rate, for crystal content between 0 and 50 % for 1 (left column) and 0.5 wt.% (right column) of dissolved H_2O; the rheology of both ideal suspensions moderately increase below 0.4 with a variation lesser than 2 log units due to T variations; from 0.4 to 0.5 viscosities strongly augment up to 8 unit log. These calculated viscosities of the suspensions were used to calculate the Reynolds number fixing the dyke width (d) to 4.3 m, using two densities (ρ) of 1,800 and 2,500 kg/m^3 (from Fig. 13) for four different ascending velocities. The end of laminar regime is fixed at 1,000, a full turbulent regime is arbitrarily set above 2,000 (see text).

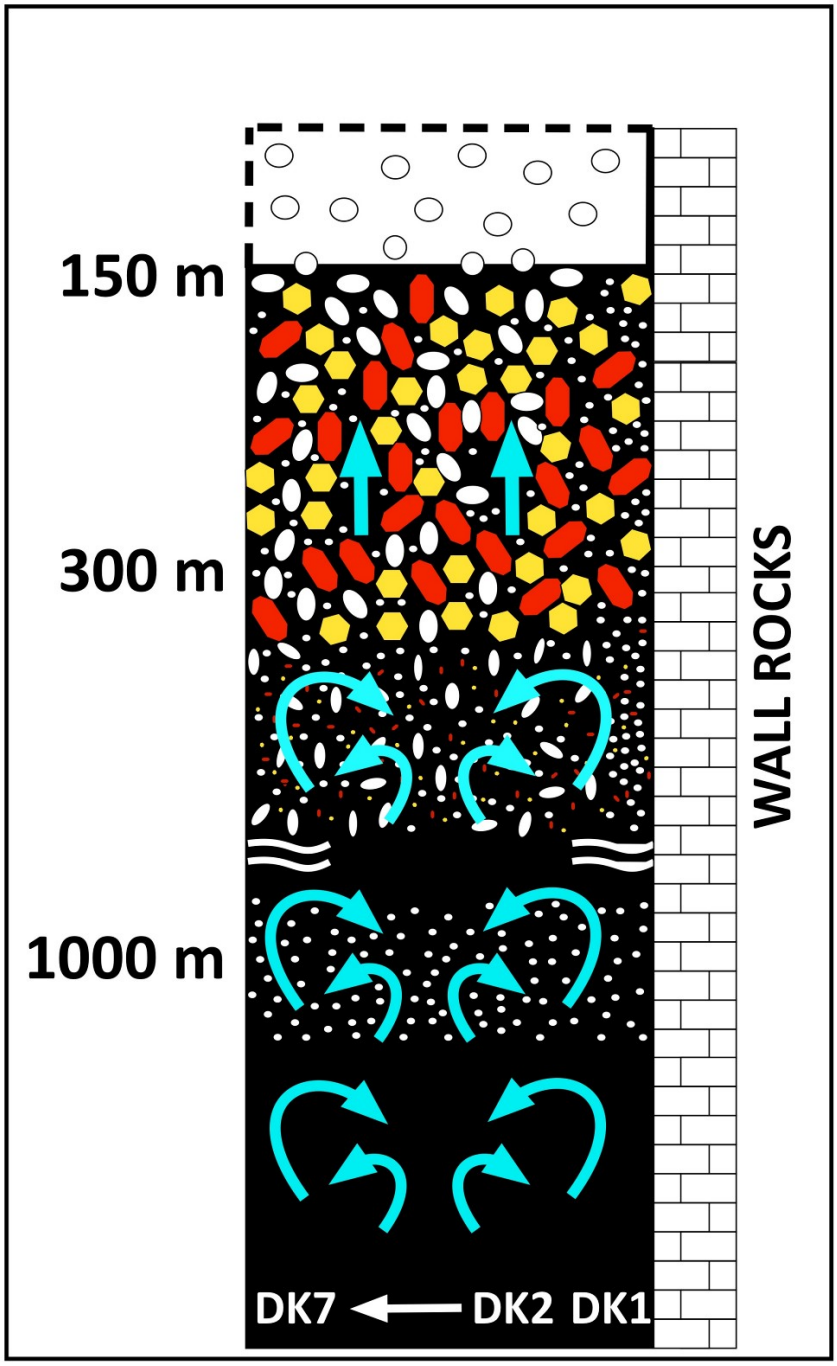

Fig. 15. Schematic cartoon resuming the nodal evolution step of the dyke magma. At P > 20 MPa the DK magma is free of crystals and bubbles, with 1 wt.% of H_2O and probably is non-laminar (cyan arrows). Between 20 and 10 MPa H_2O initiate to exsolve to form up to 30 vol.% of bubbles (tiny circular to large oblate white bubbles) under a transitional to turbulent regime; at this stage the early plg and cpx cores solidified by decompression-induced degassing (tiny red and yellow crystals); exsolution and crystallization cooperated to sluggish the DK ascent and switching the flow regime to laminar. Between 9 and 2 MPa, the most part of plg and cpx grown by cooling to attain maximum sizes of 0.1/0.2 mm that arrested any flowage. The P reported here can be transformed in depths below the ancient levels assuming a density of overlying rocks and/or magma.